# The downregulation of Kv1 channels in Lgi1 mice is accompanied by a profound modification of its interactome and a parallel decrease in Kv2 channels

Jorge Ramirez-Franco, Kévin Debreux, Marion Sangiardi, Maya Belghazi, Yujin Kim, Suk-Ho Lee, Christian Lévêque, Michael Seagar, Oussama El Far

Neurobiology of Disease 196 (2024) 106513

Contents lists available at ScienceDirect

Neurobiology of Disease

journal homepage: www.elsevier.com/locate/ynbdi

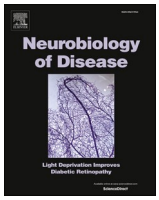

# The downregulation of $Kv_1$ channels in *Lgi1*$^{-/-}$ *mice* is accompanied by a profound modification of its interactome and a parallel decrease in $Kv_2$ channels

Jorge Ramirez-Franco [a,*], Kévin Debreux [a], Marion Sangiardi [a], Maya Belghazi [b], Yujin Kim [c], Suk-Ho Lee [c], Christian Lévêque [a], Michael Seagar [a], Oussama El Far [a,*]

[a] INSERM UMR_S 1072, Unité de Neurobiologie des canaux Ioniques et de la Synapse, Aix-Marseille Université, 13015 Marseille, France
[b] Marseille Protéomique (MaP), Plateforme Protéomique IMM, CNRS FR3479, Aix-Marseille Université, 31 Chemin Joseph Aiguier, 13009 Marseille, France
[c] Department of Physiology, Cell Physiology Lab, Seoul National University College of Medicine, 103 Daehak-ro, Jongno-gu, Seoul 03080, South Korea

ARTICLE INFO

*Keywords:*
$Kv_1$ channels
$Kv_2$ channels
Leucine-rich glioma-inactivated 1 (LGI1)
Limbic encephalitis
Autosomal-dominant lateral temporal lobe epilepsy
Proteomic

ABSTRACT

In animal models of LGI1-dependent autosomal dominant lateral temporal lobe epilepsy, $Kv_1$ channels are downregulated, suggesting their crucial involvement in epileptogenesis. The molecular basis of $Kv_1$ channel-downregulation in LGI1 knock-out mice has not been elucidated and how the absence of this extracellular protein induces an important modification in the expression of $Kv_1$ remains unknown. In this study we analyse by immunofluorescence the modifications in neuronal $Kv_{1.1}$ and $Kv_{1.2}$ distribution throughout the hippocampal formation of LGI1 knock-out mice. We show that $Kv_1$ downregulation is not restricted to the axonal compartment, but also takes place in the somatodendritic region and is accompanied by a drastic decrease in $Kv_2$ expression levels. Moreover, we find that the downregulation of these Kv channels is associated with a marked increase in bursting patterns. Finally, mass spectrometry uncovered key modifications in the $Kv_1$ interactome that highlight the epileptogenic implication of $Kv_1$ downregulation in LGI1 knock-out animals.

## 1. Introduction

The delayed rectifying $Kv_1$ channels (KCNA, Shaker) which mediate low voltage-activated $K^+$ currents are key regulators of neuronal excitability, affecting action-potential (AP) threshold and firing patterns (Johnston et al., 2010) (Jan and Jan, 2012) (Debanne et al., 2011). Functional plasticity in neurons involves dynamic changes in the expression and subcellular distribution of potassium channels in distinct neuronal compartments (Trimmer, 2015). $Kv_1$ channels are formed by homomeric or heteromeric co-assembly of four alpha subunits with auxiliary subunits (Trimmer, 2015). A subset of $Kv_1$ subunits, namely $Kv_{1.1}$ (KCNA1), $Kv_{1.2}$ (KCNA2) and $Kv_{1.6}$ (KCNA6) underlie the α-dendrotoxin (α-DTX) sensitive D-type current and these Kv subunits are present in axonal and synaptic compartments (Ogawa et al., 2008) (Gu et al., 2003) as well as at axonal initial segments (Inda et al., 2006) (Seagar et al., 2017).

Gain- or loss-of-function, inherited or de novo missense variants of these subunits lead to neurological disorders which display extensive clinical heterogeneity (Browne et al., 1994) (Herson et al., 2003) (Verdura et al., 2020) (Doring et al., 2021).

Leucine-rich glioma-inactivated 1 (LGI1) is a secreted extracellular glycoprotein (Senechal et al., 2005) which is associated with $Kv_1$ channels (Ogawa et al., 2010) (Schulte et al., 2006) (Irani et al., 2010). Mutations in the LGI1 gene often result in the inhibition of its secretion (Senechal et al., 2005) (Fukata et al., 2006), which underlies hyperexcitability in Autosomal Dominant Lateral Temporal Lobe Epilepsy (ADLTE). Also, the production of LGI1-autoantibodies promotes neuronal excitability and epilepsy in LGI1-dependent autoimmune limbic encephalitis. In both genetic and autoimmune disruption of LGI1 function, a significant decrease in total, as well as plasma membrane, $Kv_{1.1}$ and $Kv_{1.2}$ is observed (Seagar et al., 2017) (Petit-Pedrol et al., 2018) (Zhou et al., 2018). This decrease may underlie the increase in neuronal excitability in ADLTE (Seagar et al., 2017) and precedes the previously described (Fukata et al., 2021) perturbation in the AMPA/NMDA receptors ratio (Petit-Pedrol et al., 2018) (Seagar et al., 2017). An additional secretion-defective LGI1 mutation was recently found to

* Corresponding authors.
*E-mail addresses:* jose-jorge.ramirez-franco@univ-amu.fr (J. Ramirez-Franco), oussama.el-far@inserm.fr (O. El Far).

https://doi.org/10.1016/j.nbd.2024.106513
Received 8 November 2023; Received in revised form 12 March 2024; Accepted 23 April 2024
Available online 24 April 2024

induce $Kv_{1.1}$ downregulation underlying neuronal hyperexcitability and irregular spiking in the CA1 pyramidal cells (Zhou et al., 2023). Although LGI1 is part of the $Kv_1$-associated proteome (Ogawa et al., 2010) (Schulte et al., 2006) (Irani et al., 2010) (Ramirez-Franco et al., 2022), how the absence of an extracellular glycoprotein leads to the downregulation of $Kv_1$ subunits has not yet been elucidated. LGI1 binds to the proteolytically-inactive transmembrane ADAM family members ADAM11, 22 and 23 (Sagane et al., 2008) (Yamagata et al., 2018) (Owuor et al., 2009) and $Kv_1$ is a constituent of the ADAM22-associated proteome (Fukata et al., 2021). While ADAM22 (Fukata et al., 2006) as well as $Kv_{1.1}$ and $Kv_{1.2}$C-terminal tails, directly interact with Post-synaptic Density Proteins 95/93 (PSD95/93), also called Disc Large proteins 4 and 2 respectively (DLG4/2) via PDZ domains (Kim et al., 1995), the interplay between the ADAMs, PSD95/93 and Kv1 subunits is complex. PDZ interaction domains of $Kv_1$ are crucial for surface expression but not axonal targeting (Gu et al., 2003). Also, PSD93, but not PSD95 (Rasband et al., 2002) (Ogawa et al., 2010) nor ADAM22 (Ogawa et al., 2010), is important for $Kv_{1.1}$ and $Kv_{1.2}$ channel localisation and clustering at axonal initial segments (Ogawa et al., 2008).

In this study we unveil the molecular pathways by which the absence of LGI1 may trigger a decrease in the expression and mislocalization of several potassium channels at different cellular loci throughout the hippocampal formation. The use of mass spectrometry uncovered key modifications in the $Kv_1$ interactome that highlight the epileptogenic implication of Kv1 downregulation. We finally show that complex bursting patterns dominate in *Lgi1*$^{-/-}$ CA3 pyramidal neurons, and that this is associated with a substantial decrease in the somatodendritic $Kv_2$ channels that are known to participate in modulating spike bursting patterns (Raus Balind et al., 2019).

## 2. Materials and methods

### 2.1. Antibodies and other reagents

Mouse (K20/78; RRID:AB_10672854 and K36/15; RRID:AB_10673166) anti-$Kv_{1.1}$, anti-$Kv_{1.2}$ (K14/16; RRID:AB_10674277) and anti-PSD93 (N18/28; 75–057, RRID: AB_2277296) were from Antibodies Incorporated and were used for Western blots and/or immunohistofluorescence experiments. Guinea pig (386 005, RRID: AB_2737033) anti-ankyrinG (AnkG) was from Synaptic Systems and rabbit anti-$Kv_{2.1}$ (APC-012) from Alomone labs. Monoclonal JA9 anti-PMCA4 was purchased from Thermo Fisher Scientific. Secondary Alexa coupled 488-goat anti-mouse, 488-anti-rabbit, 594-goat anti-guinea pig were from Jackson ImmunoResearch. A rabbit polyclonal anti C-terminal peptide (aa 454–468) of mouse $Kv_{1.2}$ was produced and affinity purified by GeneCust and used for immunoprecipitation experiments, since monoclonal $Kv_{1.2}$ antibodies gave poor immunoprecipitation yields. This antibody was used at 5 μg/ml for Western blot analysis and 5 μg / immunoprecipitated sample. HRP-coupled secondary antibodies were from Jackson ImmunoResearch. Chemicals were purchased form Euromedex and DAPI from Sigma-Aldrich.

### 2.2. Clones

pcDNA3 plasmids containing human $Kv_{1.1}$ or rat $Kv_{1.2}$ were a generous gift from Jeffrey Martens (University of Michigan, USA). These sequences contain pHLuorin ($Kv_{1.1}$) and EGFP ($Kv_{1.2}$) coding sequences inserted in frame, in the extracellular loop linking transmembrane domains one and two. EGFP sequence in $Kv_{1.2}$ was replaced by that encoding pHLuorin, using EcoR1 and Not1 restriction sites. The full coding sequences of pHLuorine-$Kv_{1.1}$ and pHLuorine-$Kv_{1.2}$ were transferred into pINDUCER11 (gift from Stephen Elledge, Harvard Medical School, Boston, USA) plasmid downstream of a doxycycline inducible promotor. $Kv_{1.1}$, $Kv_{1.2}$, $Kv_{1.3}$ and $Kv_{1.4}$C-terminal tail constructs were generated by standard polymerase chain reaction (PCR) using a commercial adult rat brain cDNA library (OriGene Technologies, Inc). Sequences were cloned in pGEX-5× using EcoR I and *Sal* I restriction sites.

### 2.3. Bacterial recombinant protein expression and purification

GST-Kv C-terminal tail fusion constructs were transfected into the BL21 bacterial strain and recombinant protein expression induced by 0.5 mM IPTG. Bacterial pellets were resuspended and solubilised in 25 mM Tris pH 7.4, 150 mM NaCl supplemented with 1% Triton X-100 in the presence of protease inhibitors (Complete, Roche Diagnostics GmbH). Fusion proteins were purified on glutathione-Sepharose (Cytiva) using previously described procedures (Flores et al., 2019).

### 2.4. Western blots and ELISA

Western blots and ELISA experiments were performed using previously described procedures (Di Giovanni et al., 2010). For Western blots, 50 μg of proteins were loaded in each well. Signals were quantified using ImageJ and normalized to GAPDH intensities. For ELISA, 1 μg of purified GST-fusion proteins were immobilized in each well and proteins were detected using either anti-GST (1:2000) or anti-$Kv_{1.2}$ polyclonal antibody. Anti-$Kv_{1.2}$ signals were normalized to anti-GST signals on parallel wells. Western blots were performed on triplicate samples from at least 3 animals. Statistical analysis was performed using the two-sample *t*-test or two-tailed Mann-Whitney *U* test.

### 2.5. Cell culture

HEK293T cells were cultured at 37 °C in DMEM (GlutaMAX) supplemented with 10% foetal bovine serum, 1% non-essential amino acids and 1% streptomycin/penicillin mix. Transfection with pINDUCER11-$Kv_{1.1}$ or pINDUCER11-$Kv_{1.2}$ expression plasmids was performed in optiMEM using Lipofectamine 2000. Kv expression was induced by doxycycline for 48 h before cell harvesting. Cells were lysed in a Potter homogenizer using 20 mM HEPES pH 7.4, 150 mM NaCl supplemented with protease inhibitors (Complete, Roche Diagnostics GmbH). Cell membranes were harvested by a 30 min centrifugation at 16000 x*g* and resuspended in lysis buffer for protein analysis.

### 2.6. Biochemical sample preparations and immunoprecipitations

Wild type and *Lgi1*$^{-/-}$ (Chabrol et al., 2010) (the original *Lgi1*$^{-/-}$ mice strain was a generous gift from Stéphanie Baulac, ICM, Paris, France) mice total brains or hippocampi (15–16 days) were extracted, snap-frozen in liquid nitrogen and kept at −80 °C until use. Homogenisation (1 ml / brain) was performed in HB buffer (20 mM Na phosphate pH 7.4, 30 mM NaCl containing phosphatase inhibitors (Pierce™) and protease inhibitors (Complete, Roche Diagnostics GmbH) and nuclei were eliminated by 900 x*g* centrifugation. Supernatants were either directly processed for SDS-PAGE analysis and Western blot or solubilised for immunoprecipitation in HB supplemented with 1% CHAPS at 5 mg/ml and subjected to 100.000 x*g* ultracentrifugation. The solubilised material from both wildtype and *Lgi1*$^{-/-}$ samples was precleared with rProtein A Sepharose Fast Flow (Cytiva) and immunoprecipitated in triplicates, from three different animals, using the polyclonal anti-$Kv_{1.2}$ antibody (3–5 μg / immunoprecipitated sample). Immunoprecipitated samples were washed three times with HB containing 0.5% CHAPS before denaturation. Samples were then analysed either by SDS-PAGE and Western blot or by mass spectrometry. C3HeB/FeJ Kcna2 mice brains (P10) ($Kv_{1.2}^{-/-}$) and their wild type littermates (Hyun et al., 2013) were extracted and deep frozen in dry ice then transferred to −80 °C and stored until use. Homogenisation and analysis by Western blot were performed as described for WT and *Lgi1*$^{-/-}$ samples. The number of experiments performed, as well as the associated statistics are mentioned in the legends of the corresponding figures.

### 2.7. Mass spectrometry

Samples were treated and analysed as in (Ramirez-Franco et al., 2022). Briefly, immunoprecipitated proteins were concentrated and analysed by mass spectrometry using a hybrid Q-Orbitrap mass spectrometer (Q-Exactive, Thermo Fisher Scientific, United States) coupled to nanoliquid chromatography (LC) Dionex RSLC Ultimate 3000 system (Thermo Fisher Scientific, United States). All raw data files generated by MS were processed to generate mgf files and screened against the Swissprot database (Swissprot version June 2019, (560,118 sequence), with the taxonomy *Mus musculus*, using the MASCOT software (www.matrixscience.com, version 2.3). The database was searched in the decoy mode and emPAIs automatically calculated by the MASCOT algorithm. All samples were analysed in triplicates. For each antibody, background interactomes obtained with non-immune antibodies were subtracted using an Excel script. Keratins, ribosomal proteins, DNA binding proteins, mitochondrial proteins, transcriptional proteins and immunoglobulins were excluded from the list of candidates. Candidates with emPAI <0.1 were not interpreted. Functional properties of candidate proteins were classified using the pantherdb web site (www.pantherdb.org) (Supplementary sheet). The mass spectrometry proteomics data have been deposited in the ProteomeXchange Consortium via the PRIDE (Perez-Riverol et al., 2022) partner repository with the dataset identifier PXD043649.

### 2.8. Immunohistofluorescence staining of fixed brains

All experiments were performed in accordance with the European and institutional guidelines for the care and use of laboratory animals (Council Directive 86/609/EEC and French National Research Council) and approved by the local authority (Préfecture des Bouches-du-Rhône, Marseille). Mice of either sex were used in this study. Fixed brains of P14-P16 C57BL/6 wild-type mice or *Lgi1*$^{-/-}$ littermates of either sex were sliced and stained as described in (Ramirez-Franco et al., 2022). For $Kv_{1.1}$ and $Kv_{1.2}$ staining, an antigen retrieval process was applied as in (Haddjeri-Hopkins et al., 2021) (Jiao et al., 1999). Three animals per genotype were used for each of the immunohistofluorescence conditions tested.

### 2.9. Image analysis

Image analysis was performed as described in (Ramirez-Franco et al., 2022). Briefly, AnkyrinG staining was used to identify the AIS and hence to measure the immunoreactivity of $Kv_{1\cdot1}$, $Kv_{1\cdot2}$, $Kv_{2.1}$ and PSD93 in this compartment. For 3D quantification in confocal images, 3D objects counter (Bolte and Cordelieres, 2006) and 3D ROI manager (Ollion et al., 2013) were integrated into custom-written FIJI scripts available upon reasonable request. For the sake of clarity in Fig. 4E, the PSD93 signal corresponding to the AIS was extracted using the "Clear Outside" method in ImageJ after using the thresholded AnkyrinG signal as a 3D selection.

### 2.10. Acute slice preparation

Postnatal (P14) WT or *Lgi1*$^{-/-}$ mice were deeply anesthetized in isoflurane (3% in oxygen, 2l/min) and decapitated. After dissection, the brains were immersed in oxygenated (95% $O_2$, 5% $CO_2$) ice-cold low-calcium artificial CSF (aCSF) containing the following (in mM): 125 NaCl; 2.5 KCl; 1.25 $NaH_2PO_4$; 0.5 $CaCl_2$; 2 $MgCl_2$; 26 $NaHCO_3$; 10 D-Glucose; pH 7.4. Horizontal slices (350 μm) were cut in a vibratome (Leica VT1200S) in oxygenated ice-cold low-calcium aCSF. Afterwards, slices were transferred and kept at least 1 h at RT in oxygenated aCSF containing the following (in mM): 125 NaCl; 2.5 KCl; 0.8 $NaH_2PO_4$; 26 $NaHCO_3$; 3 $CaCl_2$; 2 $MgCl_2$; 10 D-Glucose; pH 7.4.

### 2.11. Electrophysiology and data analysis

Whole-cell recordings of visually identified CA3 pyramidal neurons were performed in a temperature controlled (30 °C) chamber superfused with oxygenated aCSF. Borosilicate patch pipettes (3–5 MΩ) were pulled on a DMZ-Universal Puller (Zeitz Instruments) and filled with an internal solution containing (in mM): 120 K-gluconate; 20 KCl; 10 HEPES; 0.1 EGTA; 2 $MgCl_2$; 2 $Na_2ATP$; 0.3 NaGTP; pH 7.4; 290–300 mOsm. Recordings were made in current clamp mode with a multiclamp 700B amplifier (Molecular Devices) and pClamp10 software. Recordings were acquired at 10 kHz and filtered at 3 kHz. Neurons with a resting membrane potential > -55 mV were discarded from the final analysis. Intrinsic excitability was assessed by injecting a range of 0.8 s current pulses (ranging from −50 to 250 pA; 10 pA / step) and counting the number of spikes. Input–ouput curves were determined and the rheobase was defined as the minimal current eliciting at least one action potential. To study bursting propensity, depolarizing current injections of 0.5 s (300 or 600 pA) were applied every 2 s. Bursts were scored when ≥2 APs appeared in the same response showing progressively smaller amplitude and longer duration (Raus Balind et al., 2019). To analyse the proportion of cells exhibiting complex bursts, only cells showing bursts at the rheobase current injection were considered. To study burst propensity, only cells exhibiting bursts when challenged with either 300 pA or 600 pA depolarizing pulses were defined as positive. AP parameters (AP half-width and AP amplitude) were extracted from the first spike in the rheobase. To prevent synaptic contamination 3 mM kynurenate and 100 μM picrotoxin (both from SIGMA) were systematically added to the aCSF. Cells were held at ~ −70 mV during experiments and recordings were not corrected for liquid junction potential. All data were analysed using ClampFit (Molecular Devices). Data are presented as mean ± SEM. Mann–Whitney *U* test, Two samples *t*-test, and Fisher's exact test were used for comparisons. Normality tests were applied before the use of the Mann-Whitney U test or Two samples t-test. The number of experiments performed, as well as the associated statistics are mentioned in the legends of the corresponding figures. For rheobase analyses WT $n = 30$ cells from 8 animals; KO $n = 35$ cells from 8 animals. For bursting propensity analyses WT $n = 8$ cells from 2 animals; KO n = 8 cells from 4 animals.

## 3. Results

### 3.1. $Kv_{1.1}$ and $Kv_{1.2}$ expression in *Lgi1*$^{-/-}$

We have previously shown that $Kv_{1.1}$ and $Kv_{1.2}$ subunits were massively downregulated in LGI1 knock-out mice (*Lgi1*$^{-/-}$) total brain extracts and that, in this genetic background, $Kv_{1.1}$ was almost absent from axonal initial segments of hippocampal and cortical neurons (Seagar et al., 2017). In the light of the major enrichment of LGI1 in the hippocampal formation (Ramirez-Franco et al., 2022), we compared by Western blot the downregulation level of $Kv_{1.1}$ and $Kv_{1.2}$ subunits in total brain homogenates as well as in hippocampal extracts (Figs. 1 and 2). The decrease in expression of $Kv_{1.1}$ and $Kv_{1.2}$ in total brain (Fig. 1A) ($Kv_{1.1}$ WT 1.00 ± 0.07 vs $Kv_{1.1}$ *Lgi1*$^{-/-}$ 0.72 ± 0.08, $p = 0.047$; $Kv_{1.2}$ WT 1.00 ± 0.05 vs $Kv_{1.2}$ *Lgi1*$^{-/-}$ 0.52 ± 0.04, $p = 1.03 \times 10^{-7}$) was less severe than in hippocampus (Fig. 1B, $Kv_{1.1}$ WT 1.00 ± 0.05 vs $Kv_{1.1}$ *Lgi1*$^{-/-}$ 0.55 ± 0.03, $p = 1.33 \times 10^{-7}$; $Kv_{1.2}$ WT 1.00 ± 0.04 vs $Kv_{1.2}$ *Lgi1*$^{-/-}$ 0.38 ± 0.02, $p = 1.73 \times 10^{-13}$).

In order to address $Kv_1$ expression and distribution profile, we investigated, the detailed comparative immunofluorescence staining of $Kv_{1.1}$ and $Kv_{1.2}$ in the hippocampus in both WT and *Lgi1*$^{-/-}$ backgrounds. It is noteworthy that conventional immunohistochemical techniques could render the epitopes of $Kv_{1.1}$ and $Kv_{1.2}$ inaccessible to antibodies, especially in slices from prefixed brain, precluding detection of these channels particularly in the AIS of hippocampal neurons (Lorincz and Nusser, 2008b). In our hands, this proved to be the case, since $Kv_{1.1}$ was not detected in the absence of antigen retrieval protocols

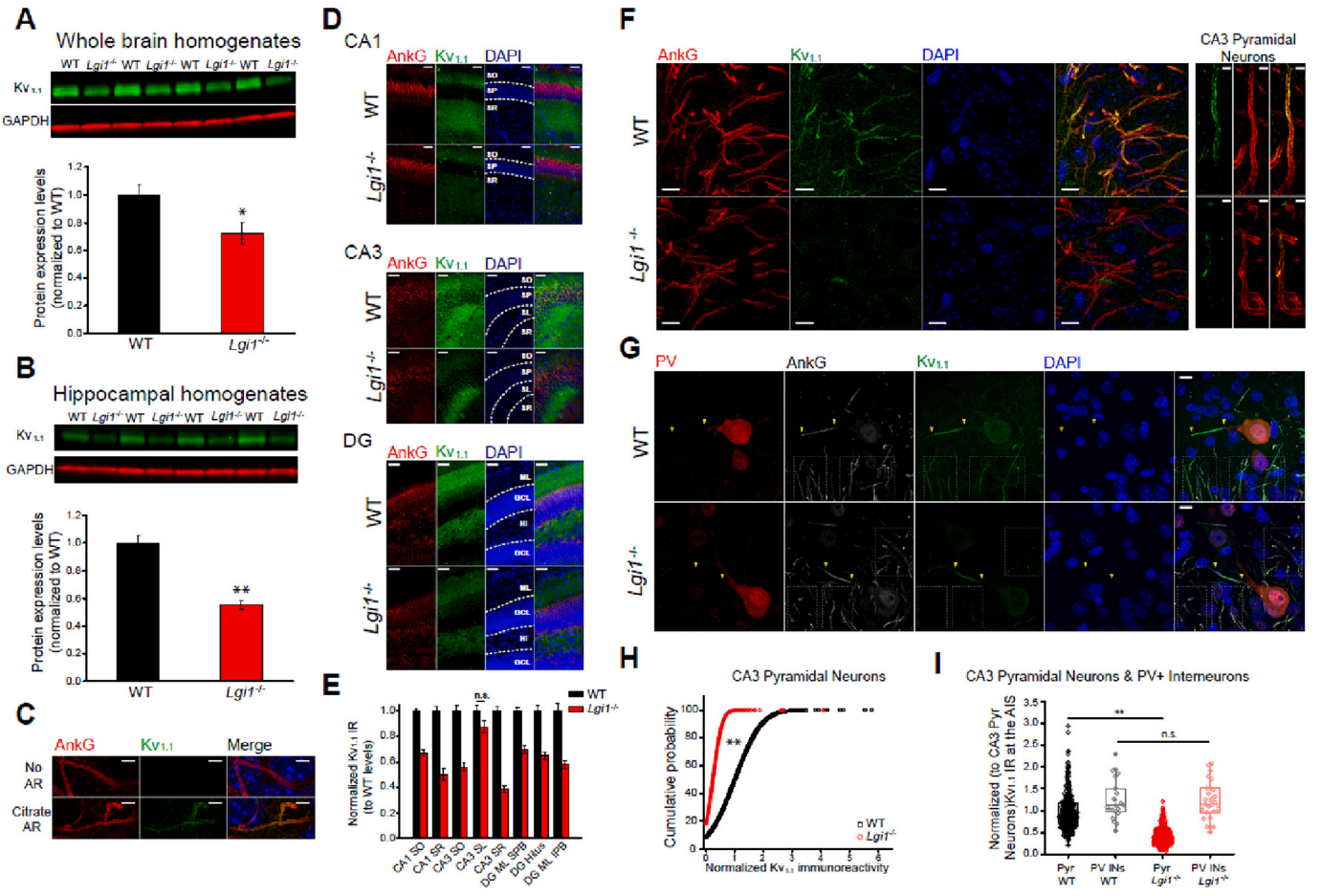


**Fig. 1.** $Kv_{1.1}$ expression is reduced in $Lgi1^{-/-}$ mice.
**(A)** Quantification by Western blot of $Kv_{1.1}$ expression in whole brain homogenates of WT (1.00 ± 0.07) and $Lgi1^{-/-}$ (0.72 ± 0.08), p = 0.047; $n = 4$; Two-sample *t*-test). **(B)** Quantification by Western blot of $Kv_{1.1}$ expression in hippocampal homogenates of WT (1.00 ± 0.05) and $Lgi1^{-/-}$ (0.55 ± 0.03); $p = 1.33 \times 10^{-7}$; $n = 16$; Two-sample t-test). In a and b, signals were normalized to GAPDH expression levels. **(C)** Representative AISs of CA3 pyramidal cells (see Supplementary Fig. S1 for larger fields of view) highlighting the necessity of antigen retrieval (bottom panels) for $Kv_{1.1}$ detection in the hippocampus. Scale bar 5 μm **(D)** Representative images of $Kv_{1.1}$ immunoreactivity (IR) across CA1 (top panels, Scale bar = 50 μm), CA3 (middle panels, Scale bar = 50 μm), and DG (bottom panels, Scale bar = 50 μm) in WT vs $Lgi1^{-/-}$ mouse. SO: Str. Oriens; SP: Str. Pyramidale; SR: Str. Radiatum; SL: Str. Lucidum; ML: Mol. Layer; GCL: Granule Cell Layer; Hi: Hilus. **(E)** Quantification of the differences in the normalized $Kv_{1.1}$ IR (to WT levels) through the different hippocampal strata. For the sake of clarity, only non-significant comparisons are indicated. For all other comparison $^{**}p < 0.01$ (CA1-SO WT = 1.00 ± 0.02 vs $Lgi1^{-/-}$ = 0.66 ± 0.02 $p = 5.96 \times 10^{-13}$; CA1-SR WT = 1.00 ± 0.03 vs $Lgi1^{-/-}$ = 0.05 ± 0.05 $p = 1.20 \times 10^{-6}$; CA3-SO WT = 1.00 ± 0.04 vs $Lgi1^{-/-}$ = 0.53 ± 0.03 $p = 2.75 \times 10^{-10}$; CA3-SL WT =1.00 ± 0.05 vs $Lgi1^{-/-}$ = 0.88 ± 0.05 $p = 0.07$; CA3-SR WT = 1.00 ± 0.03 vs $Lgi1^{-/-}$ = 0.39 ± 0.02 $p = 2.34 \times 10^{-10}$; DG-ML-SPB WT = 1.00 ± 0.02 vs $Lgi1^{-/-}$ = 0.70 ± 0.03 $p = 1.20 \times 10^{-8}$; DG-Hilus WT = 1.00 ± 0.04 vs $Lgi1^{-/-}$ = 0.65 ± 0.03 $p = 3.57 \times 10^{-8}$; DG-ML-IPB WT = 1.00 ± 0.06 vs $Lgi1^{-/-}$ = 0.58 ± 0.03 $p = 1.03 \times 10^{-7}$; Two-sample t-test). **(F)** Left, 63× images of $Kv_{1.1}$ immunoreactivity at CA3 AIS in WT (top panels) and $Lgi1^{-/-}$ (bottom panels). Scale bar = 10 μm. Right, detail of a CA3 pyramidal neuron AIS in WT (top panels) and $Lgi1^{-/-}$ (bottom panels). Scale bar = 2.5 μm. **(G)** 63× images showing no differences in $Kv_{1.1}$ IR at the AIS of PV+ interneurons delimited by yellow arrowheads. Of note, the $Kv_1$ signal in the surrounding pyramidal neurons AIS (dotted-line rectangles) is severely decreased. Scale bar = 10 μm **(H)** Cumulative probability plots of $Kv_{1.1}$ immunoreactivity at individual AIS of WT (black squares) and $Lgi1^{-/-}$ (red circles) CA3 pyramidal neurons (WT Pyr CA3 neurons = 1.00 ± 0.02 vs $Lgi1^{-/-}$ CA3 Pyr neurons = 0.23 ± 0.01; $p = 0.00$, Kolmogorov-Smirnov Test). **(I)** Comparisons of $Kv_{1.1}$ immunoreactivity (Normalized to WT CA3 Pyr neurons) at the AIS of pyramidal cells (dark tones) and PV+ interneurons (light tones) across WT (black) and $Lgi1^{-/-}$ (red) hippocampi (Pyr WT = 1.00 ± 0.02 vs Pyr $Lgi1^{-/-}$ = 0.40 ± 0.01 $p = 2.43 \times 10^{-132}$; PV+ IN WT = 1.25 ± 0.10 vs PV+ IN $Lgi1^{-/-}$ = 1.22 ± 0.08; $p = 1.00$; ANOVA followed by Bonferroni's test for means comparison).

(Fig. 1C and Supplementary Fig. S1). The use of the same antibody on organotypic slices (Extremet et al., 2023) or using mild fixation conditions in thin slices (Petit-Pedrol et al., 2018) could facilitate epitope access. Due to the tortuosity of the AIS in CA3, we chose to use 50 μm thick sections and therefore employed antigen retrieval techniques (Jiao et al., 1999) (Haddjeri-Hopkins et al., 2021) to address $Kv_{1.1}$ (Fig. 1C-H) and $Kv_{1.2}$ (Fig. 2C-H) distribution. In addition to the previously reported decrease in $Kv_1$ expression in the AIS (Fig. 1E and Fig. 2E), we observed an overall decrease in all hippocampal strata (CA1, CA3 and DG) (Fig. 1C, D, G and Fig. 2C, D, G) with a more prominent decrease of $Kv_{1.2}$ versus $Kv_{1.1}$. Interestingly, we observed that in parvalbumin (PV) positive interneurons, the expression levels of both $Kv_{1.1}$ and $Kv_{1.2}$ subunits were not affected compared to the surrounding pyramidal neurons AIS, (Fig. 1F, H and Fig. 2F, H) suggesting that $Kv_1$ expression levels in PV+ cells are not regulated by LGI1.

### 3.2. *Characterization of $Kv_{1.2}$ antibodies used for immunoprecipitation*

In order to address changes in the $Kv_{1.2}$ proteome between WT and $Lgi1^{-/-}$, we generated a polyclonal antibody directed against a C-terminal peptide sequence and performed immunoprecipitations followed by mass spectrometry analysis. As shown in Fig. 3B, this antibody recognizes $Kv_{1.2}$ from brain extracts as well as recombinant pHLuorin-tagged full length $Kv_{1.2}$, but not $Kv_{1.1}$ expressed in HEK cells. However, the band recognized in wild-type mice brain extracts was still present in $Kv_{1.2}$ knock out extracts (Fig. 3C) suggesting that this antibody can

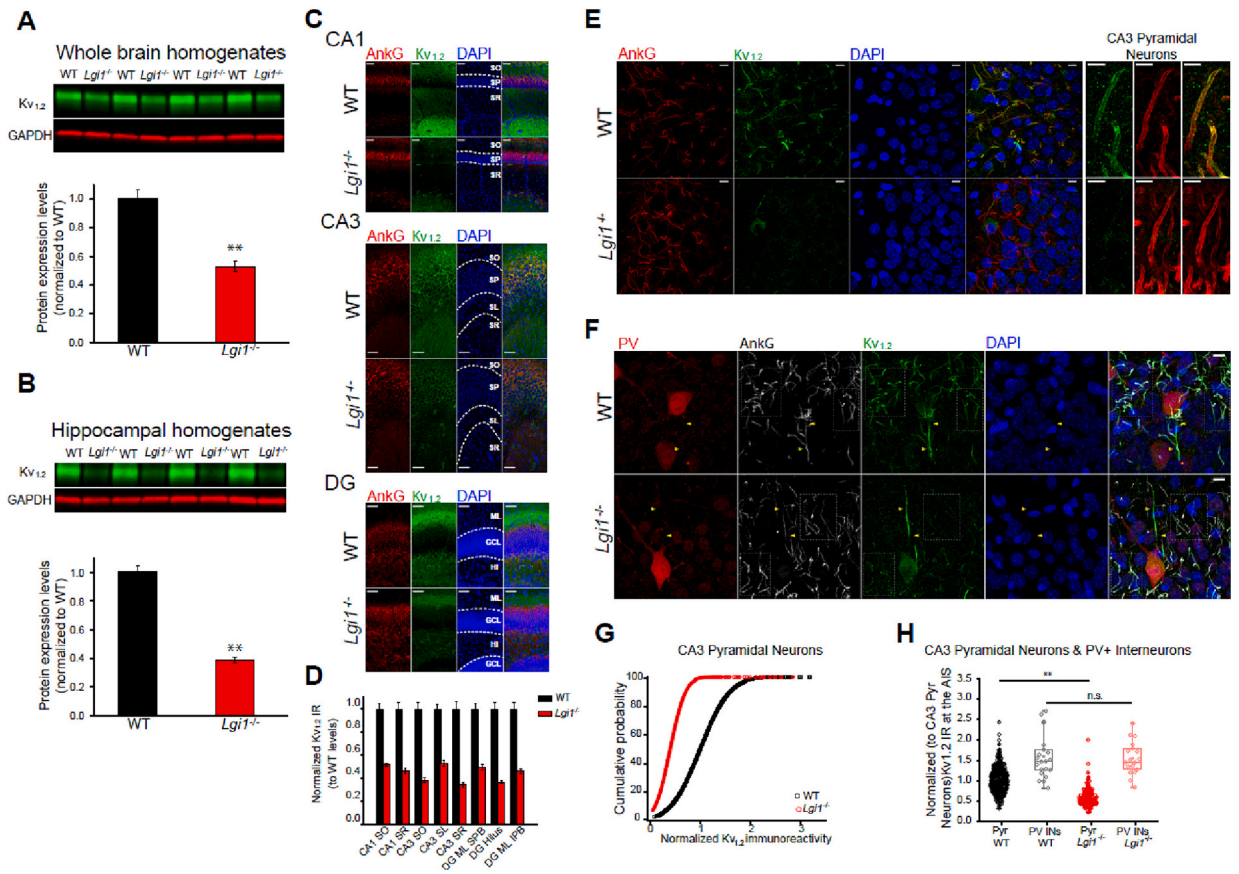


**Fig. 2.** $Kv_{1.2}$ expression is reduced in the *Lgi1*$^{-/-}$ mice.
**(A)** Quantification by Western blot of $Kv_{1.2}$ expression in brain homogenates of WT (1.00 ± 0.06) and *Lgi1*$^{-/-}$ (0.52 ± 0.04), $p = 1.03 \times 10^{-7}$; $n = 17$; Two-sample *t*-test). **(B)** Quantification by Western blot of $Kv_{1.2}$ in in hippocampal homogenates of WT (1.00 ± 0.04) and *Lgi1*$^{-/-}$ (0.38 ± 0.02); $p = 1.73 \times 10^{-13}$; $n = 20$; Two-sample t-test). In **a** and **b**, signals were normalized to GAPDH expression levels. **(C)** representative images of $Kv_{1.2}$ immunoreactivity (IR) across CA1 (top panels, Scale bar = 50 μm), CA3 (middle panels, Scale bar = 50 μm), and DG (bottom panels, Scale bar = 50 μm) in WT vs *Lgi1*$^{-/-}$ mouse. SO: Str. Oriens; SP: Str. Pyramidale; SR: Str. Radiatum; SL: Str. Lucidum; ML: Mol. Layer; GCL: Granule Cell Layer; Hi: Hilus. **(D)** Quantification of the differences in the normalized $Kv_{1.2}$ IR (to WT levels) through the different hippocampal strata, all comparisons are $^{**}p < 0.01$ (CA1-SO WT = 1.00 ± 0.04 vs *Lgi1*$^{-/-}$ = 0.52 ± 0.02 $p = 1.58 \times 10^{-13}$; CA1-SR WT = 1.00 ± 0.06 vs *Lgi1*$^{-/-}$ = 0.46 ± 0.02 $p = 8.37 \times 10^{-10}$; CA3-SO WT = 1.00 ± 0.06 vs *Lgi1*$^{-/-}$ = 0.38 ± 0.02 $p = 6.32 \times 10^{-11}$; CA3-SL WT = 1.00 ± 0.04 vs *Lgi1*$^{-/-}$ = 0.53 ± 0.03 $p = 9.61 \times 10^{-13}$; CA3-SR WT = 1.00 ± 0.06 vs *Lgi1*$^{-/-}$ = 0.34 ± 0.02 $p = 7.49 \times 10^{-11}$; DG-ML-SPB WT = 1.00 ± 0.05 vs *Lgi1*$^{-/-}$ = 0.49 ± 0.02 $p = 1.92 \times 10^{-11}$; DG-Hilus WT = 1.00 ± 0.05 vs *Lgi1*$^{-/-}$ = 0.37 ± 0.01 $p = 4.15 \times 10^{-12}$; DG-ML-IPB WT = 1.00 ± 0.05 vs *Lgi1*$^{-/-}$ = 0.46 ± 0.02 $p = 1.83 \times 10^{-10}$; Two-sample t-test). **(E)** Left, 63× images of Kv1.2 immunoreactivity at CA3 Axonal Initial segments in WT (top panels) and *Lgi1*$^{-/-}$ (bottom panels). Scale bar = 10 μm. Right, detail of a CA3 pyramidal neuron AIS in WT (top panels) and *Lgi1*$^{-/-}$ (bottom panels). Scale bar = 2.5 μm. **(F)** 63× images showing no differences in $Kv_{1.2}$ IR at the AIS of PV+ interneurons. Scale bar = 10 μm **(G)** Cumulative probability plots of $Kv_{1.2}$ immunoreactivity at individual AIS of WT (black squares) and *Lgi1*$^{-/-}$ (red circles) CA3 pyramidal neurons (WT Pyr CA3 neurons = 1.00 ± 0.01 vs *Lgi1*$^{-/-}$ CA3 Pyr neurons = 0.41 ± 0.01; $p = 0.00$, Kolmogorov-Smirnov Test). **(H)** Comparisons of $Kv_{1.2}$ immunoreactivity (Normalized to WT CA3 Pyr Neurons) at the AIS of pyramidal cells (dark tones) and PV+ interneurons (light tones) across WT (black) and *Lgi1*$^{-/-}$ (red) hippocampi (Pyr WT = 1.00 ± 0.02 vs Pyr *Lgi1*$^{-/-}$ = 0.55 ± 0.01 $p = 7.90 \times 10^{-60}$; PV+ IN WT = 1.57 ± 0.12 vs PV+ IN *Lgi1*$^{-/-}$ = 1.53 ± 0.09; $p = 1.00$; ANOVA followed by Bonferroni's test for means comparison).

cross-react, in native tissues, with closely homologous $Kv_1$ isoforms. Due to the significant sequence homology between the target peptide sequence in other $Kv_1$ family members (Fig. 3A), we verified whether at higher protein concentrations, the antibody can recognize other $Kv_1$ family members. As shown in Fig. 3E,F the antibody showed cross-reactivity with GST fusion proteins containing C-terminal sequences of $Kv_{1.1}$ and to a lesser extent $Kv_{1.3}$ but not $Kv_{1.4}$.

### 3.3. *$Kv_1$-associated proteome in WT versus Lgi1*$^{-/-}$ *brain homogenate*

The capacity of our antibody to recognize $Kv_{1.2}$ and to a lesser extent $Kv_{1.1}$ allows us to address the consequences of the absence of LGI1 on the modification of the proteome associated with these hetero-multimeric potassium channels. $Kv_1\alpha$ (KCNA1 and 2) subunits as well as other Kvβ1 (KCAB1) and β2 (KCAB2) were equally recovered, except $Kv_{1.6}$ (KCNA6) that was ~~less~~ immunoprecipitated to a lesser extent (−32,8%) from *Lgi1*$^{-/-}$ *extracts* (Table S1, and Supplementary sheet).

#### 3.3.1. *Lost $Kv_1$ partners in Lgi1*$^{-/-}$ *samples*

The most striking observation was that the landscape of the $Kv_1$ links with the cytoskeleton showed major rearrangements (Supplementary Tables S2, S3, Supplementary Fig. S2 and Supplementary sheet). The association with ACTC Actin (alpha cardiac muscle 1), the most abundant $Kv_1$ partner from WT extracts was lost in the *Lgi1*$^{-/-}$ samples. This actin isoform was shown to be widely expressed in the hippocampus and other brain structures (Magdaleno et al., 2006). In addition to actin, the co-immunoprecipitation of myosin 10 and the intermediate filament vimentin as well as the actin remodelling protein CYFP2 (cytoplasmic FMR1 Interacting Protein 2 also known as PIR12) (Zhang et al., 2019) (Chen et al., 2014) were completely disrupted in *Lgi1*$^{-/-}$. Interestingly, CYFP2 is linked to mTORC signalling (Manigandan and Yun, 2022) and was shown to be involved in epileptic encephalopathy and intellectual disability (Lee et al., 2020). The perturbations in membrane expression and cytoskeletal links of $Kv_1$ are also reflected by the loss of interaction of $Kv_1$ with the following partners: i- the membrane-associated

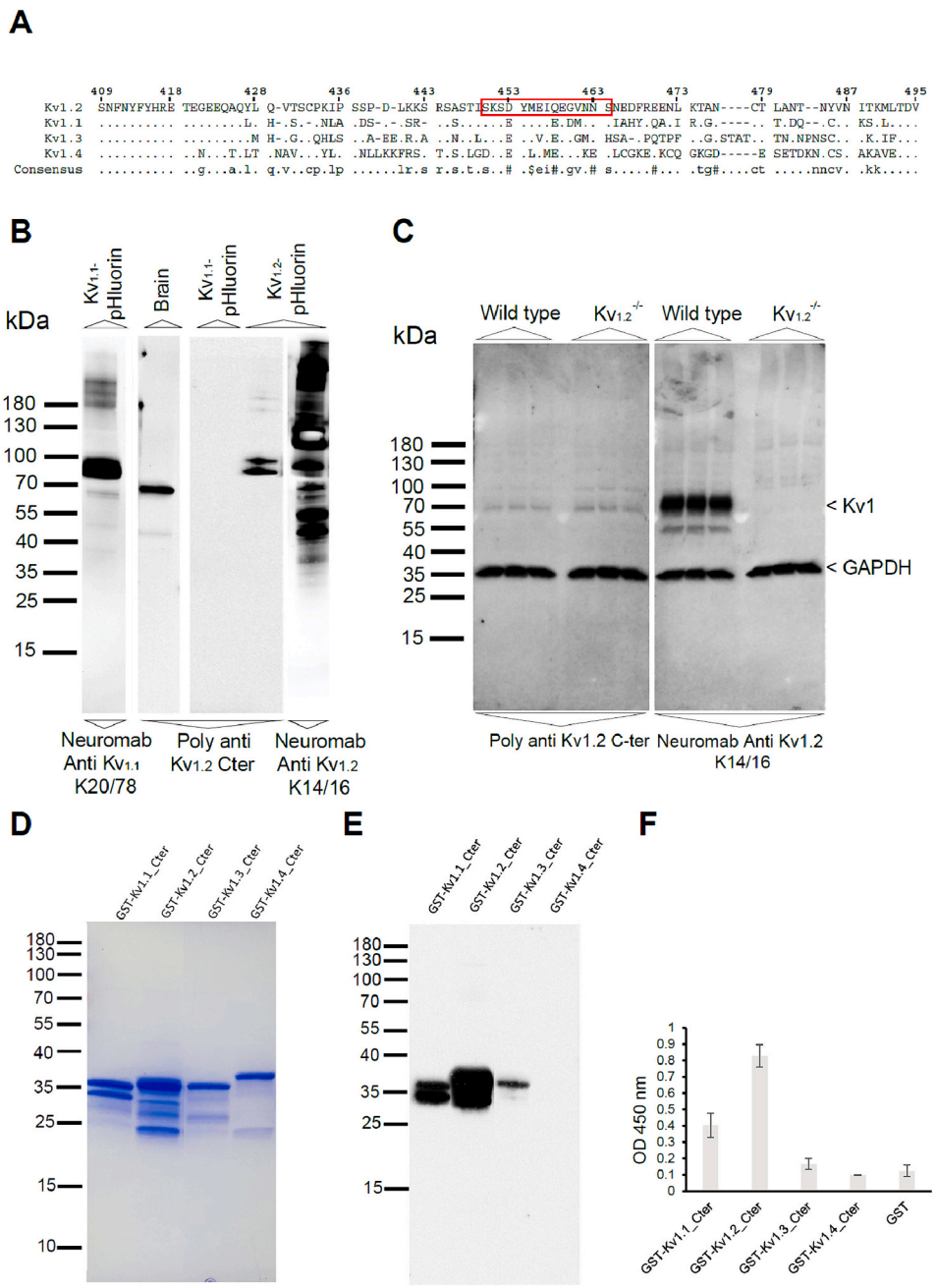


**Fig. 3.** Characterization of the rabbit polyclonal $Kv_{1.2}$ antibody.
Isoform specificity of the rabbit polyclonal $Kv_{1.2}$ antibody. **(A)** Alignment of the amino acid sequences of C-terminal tails of mice $Kv_{1.1}$, $Kv_{1.2}$, $Kv_{1.3}$, $Kv_{1.4}$. The peptide sequence that served to generate the antibody is boxed. **(B)** HEK cell extracts transfected with recombinant $Kv_{1.1}$ and $Kv_{1.2}$ as well as brain homogenates were probed with the polyclonal $Kv_{1.2}$ antibody. Control recombinant channels expression were performed using the Neuromab $Kv_{1.1}$ and $Kv_{1.2}$ antibodies. I*solated Western blot strips are from distinct gels* **(C)** Western blots of wild type and $Kv_{1.2}$ KO ($Kv_{1.2}^{-/-}$) brain homogenates with the rabbit polyclonal $Kv_{1.2}$ antibody showing cross-reactivity with closely related native $Kv_1$ channels. **(D)** Coomassie staining of the different GST fusion protein constructs (3 μg) used for western blot. **(E)** and **(F)** Western blot (300 ng/well) and ELISA (0.5 μg/well) respectively of the constructs shown in b with the polyclonal $Kv_{1.2}$ antibody showing a cross-reactivity of this antibody with $Kv_{1.1}$ and to very slight extent with $Kv_{1.3}$.

phosphatidylinositol (4,5)-bisphosphate binding protein GSDMA, that is involved in cell death and has pore forming properties (Ding et al., 2016), ii-the deltex E3 ubiquitin-protein ligase and regulator of Notch signalling DTX1, iii- the multi-modular scaffolding protein RANB9 that is implicated in actin cytoskeletal rearrangement (Valiyaveettil et al., 2008) and the integration of a variety of cell surface receptor signalling through intracellular targets (Murrin and Talbot, 2007), iv- The plasma membrane /endoplasmic reticulum (PM/ER) cholesterol transporter and phosphatidylserine binding protein (Sandhu et al., 2018) ASTRA that may indicate a change in the lipidic environment of $Kv_1$. Although a similar function was attributed to ASTRA and B, the decrease of interaction with $Kv_1$ was restricted to ASTRA, ASTRB remaining stable, v- the NEB2 (spinophilin) (Molina-Pinelo et al., 2011), a PDZ-domain containing F-actin binding and phosphatase recruiter scaffolding protein.

Intriguingly, a loss of association with PSD93 but not with its twin PSD95 or other MAGUKs was observed in *Lgi1*$^{-/-}$. We therefore investigated by Western blot and immunofluorescence whether the loss of association with PSD93 is accompanied by a decrease in its total

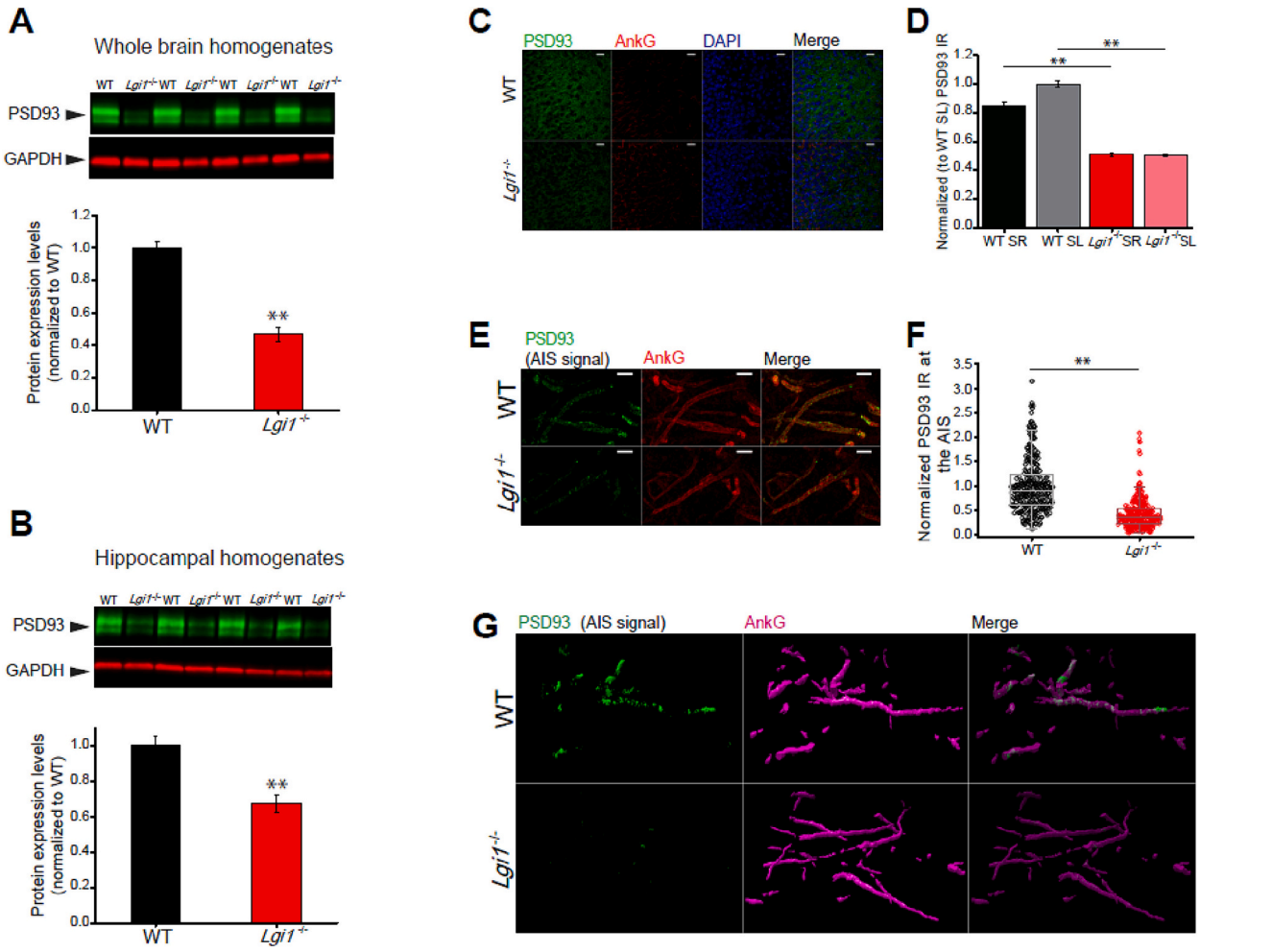


**Fig. 4.** PSD93 expression is reduced in the *Lgi1*$^{-/-}$ mice.
**(A)** Quantification by Western blot of PSD93 expression in brain homogenates of PSD93 in WT (1.00 ± 0.03) and *Lgi1*$^{-/-}$ (0.46 ± 0.04); p = 1.40 × $10^{-11}$; *n* = 20; Two-sample *t*-test). **(B)** Quantification by Western blot of PSD93 expression in hippocampal homogenates in WT (1.00 ± 0.05) and *Lgi1*$^{-/-}$ (0.68 ± 0.05); p = 6.10 × $10^{-5}$; n = 20; Two-sample t-test). In A and B, signals were normalized to GAPDH expression levels. **(C)** 25× representative images of Hippocampal CA3 region showing a decrease in PSD93 expression. PSD93 is in green, AnkyrinG is in red, and DAPI is in blue. Scale bar = 25 μm. **(D)** Quantification of PSD93 expression decrease across different CA3 regions in WT (black tones) and *Lgi1*$^{-/-}$ (red tones) normalized to WT-SL (CA3-SR WT = 0.85 ± 0.02 vs *Lgi1*$^{-/-}$ = 0.51 ± 0.01; *p* = 9.65 × $10^{-34}$; CA3-SR WT = 1.00 ± 0.02 vs *Lgi1*$^{-/-}$ = 0.50 ± 0.01; *p* = 1.31 × $10^{-63}$; ANOVA followed by Bonferroni's test for means comparison). **(E)** 63× representative images showing a reduction in PSD93 expression at the AIS level of CA3 Pyramidal neurons in *Lgi1*$^{-/-}$; PSD93 is in green and AnkyrinG is in red; Scale bar = 5 μm. **(F)** Quantification of the decreased PSD93 expression at the AIS level in *Lgi1*$^{-/-}$ hippocampal CA3 pyramidal neurons (WT = WT 1.00 ± 0.03 vs Kv1.1 *Lgi1*$^{-/-}$ 0.42 ± 0.02, *p* = 0; Mann-Whitney *U* test). **(G)** Surface representation of PSD93 labelling at the AIS of CA3 pyramidal neurons in WT (top panels) and *Lgi1*$^{-/-}$ (bottom panels) hippocampi. Magenta: AnkG, Green: PSD93.

expression level. As shown in Fig. 4, PSD93 expression levels were severely downregulated in *Lgi1*$^{-/-}$ samples with a more prominent decrease in total brain homogenates (PSD93 WT 1.00 ± 0.03 vs PSD93 *Lgi1*$^{-/-}$ 0.46 ± 0.04, $p = 1.40 \times 10^{-11}$) (Fig. 4A) compared to hippocampal extracts (PSD93 WT 1.00 ± 0.05 vs PSD93 *Lgi1*$^{-/-}$ 0.68 ± 0.05, $p = 6.10 \times 10^{-5}$) (Fig. 4B). A closer look at the subcellular distribution of PSD93 indicates that this decrease was not restricted to the AIS (Fig. 4E, F) and was observed also in the stratum radiatum (SR) and stratum lucidum (SL) of CA3 (Fig. 4C, D). Finally, the association of $Kv_1$ with the myelin proteolipid protein (MYPR), a major determinant in the formation and maintenance of the multilamellar structure of myelin was also lost in *Lgi1*$^{-/-}$. All these molecular signatures indicate a drastic change in $Kv_1$ membrane and sub-membrane associated complexes and corroborate the significant downregulation of membranous $Kv_1$ (Seagar et al., 2017).

### 3.3.2. *New $Kv_1$ partners in Lgi1*$^{-/-}$ *samples*

*In parallel to* the loss of all the above mentioned membranous, submembranous and cytoskeletal links of $Kv_1$, we found that, in *Lgi1*$^{-/-}$ (Supplementary Table S3), $Kv_1$ engaged novel molecular interactions and showed association with the microtubule associated protein doublecortin (DCX) and with the GTPases Septin 6 and 7 that are involved in actin and microtubule cytoskeleton organisation, membrane trafficking, vesicle transport and exocytosis, as well as the assembly of scaffolding platforms (Neubauer and Zieger, 2017) (Spiliotis, 2018). Interestingly, Septin 6 has been shown to be localized at the neck of dendrites (Cho et al., 2011), suggesting a potential reorganisation of $Kv_1$ localization. In addition, we found that in *Lgi1*$^{-/-}$ samples, $Kv_1$ ~~is~~ was associated with the calcium sensor Copine 6 that regulates structural plasticity of spines. Despite the loss of interaction with actin, $Kv_1$ in *Lgi1*$^{-/-}$ acquired association with the filamentous protein and actin-crosslinking MARCS (Myristoylated alanine-rich C-kinase substrate).

*3.3.3. Significant changes in the association of some $Kv_1$ partners in $Lgi1^{-/-}$ samples*

Among $Kv_1$ partners that were immunoprecipitated from both wild type and $Lgi1^{-/-}$ extracts, those that varied less than ±20% were considered stable. ADAM22 (Disintegrin and metalloproteinase domain-containing protein 22) association was by far the most affected partner with over 60% decrease followed by PSD95 > SAP97 (DLG1) > SAP102 (DLG3) with >50%, > 44% and 40% decrease respectively. Although both ADAM22 and ADAM23 co-immunoprecipitated $Kv_{1.2}$ from pre-enriched LGI1-associated complexes (Fukata et al., 2010), and both proteins associate with LGI1 (Ramirez-Franco et al., 2022), ADAM23 was totally absent from our immunoprecipitations from both WT and $Lgi1^{-/-}$ samples.

Beside these partners that show decreased association with $Kv_1$, an important increase in channel association with several key proteins was observed. The biggest increase in interaction (> 127%) was observed for 14–3-3γ (Ywhag). This increase is accompanied by a > 55% augmentation of interaction with 14–3-3ε. The second largest increase (> 77%) concerned the vesicle-associated membrane protein-associated protein A (VAPA) tether protein but not VAPB that remained rather stable. In parallel to these differences, there was a noticeable increase of association with the cytosol aminopeptidase AMPL and the leucine-rich repeat and transmembrane domain-containing protein 2 (LRTM2), which are involved in axon guidance. It is interesting to note that while the interaction of $Kv_1$ with the serine/threonine-protein phosphatase 2B catalytic subunit beta isoform (PP2BB) is lost, the one with the alpha isoform (PP2BA) increases by >34%. In parallel to the interaction with Septin 6 and 7 mentioned earlier, an increase of interaction with Septin 11 was observed. Septin 11 (SEP11), is enriched post-synaptically at the neck of dendritic spines at GABAergic synapses (Li et al., 2009). This observation suggests a reorganisation in the dendritic localisation of $Kv_1$. Among the partners with increased association with $Kv_1$, we found WD repeat-containing protein 26 (WDR26) which is a G-beta-like negative regulator of MAPK pathway, haploinsufficiency of which induces among other symptoms intellectual disability and seizures (Skraban et al., 2017). Interestingly, the LGI1 EPTP domain shows

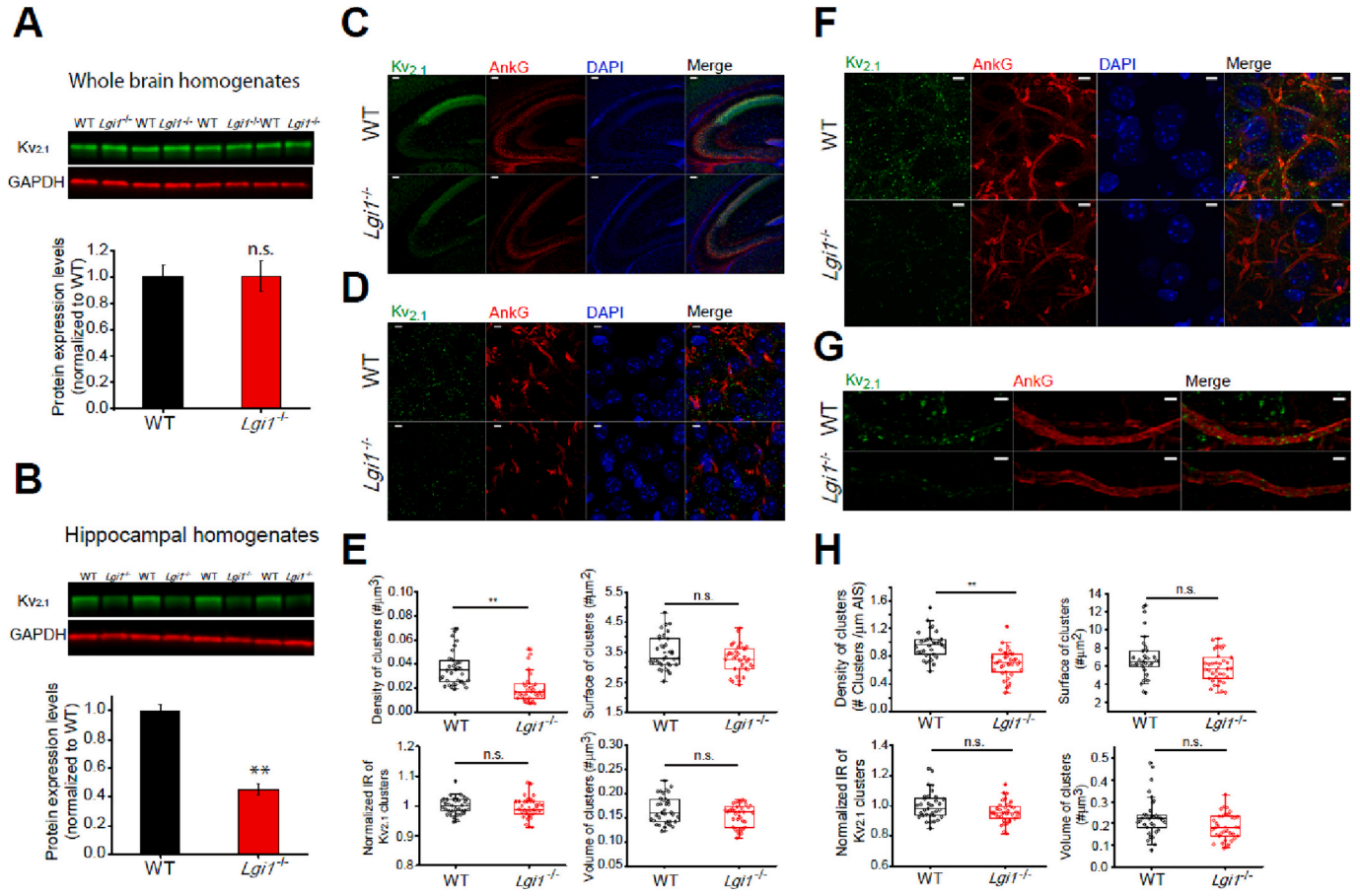


**Fig. 5.** $Kv_{2.1}$ is selectively reduced in hippocampus of $Lgi1^{-/-}$ mice.
**(A)** Quantification by Western blot of $Kv_{2.1}$ expression in brain homogenates of WT (WT 1.00 ± 0.09) and $Lgi1^{-/-}$ (1.01 ± 0.11); p = 0.97; $n = 15$; Two-sample *t*-test). **(B)** Quantification by Western blot of $Kv_{2.1}$ expression in WT (1.00 ± 0.04) and $Lgi1^{-/-}$ (0.45 ± 0.04) hippocampal extracts; p = 1.00 × $10^{-9}$; $n = 16$; Two-sample t-test). **(C)** 10× representative images showing a reduced expression of $Kv_{2.1}$ across the hippocampus of $Lgi1^{-/-}$ mouse. Scale bar = 100 µm. **(D)** Representative 63× images showing a reduction of $Kv_{2.1}$ in CA3 Str. Pyramidale of $Lgi1^{-/-}$ hippocampus. Scale bar = 5 µm. **(E)** Analysis of $Kv_{2.1}$ puncta in CA3 in WT (black) and $Lgi1^{-/-}$ (red) hippocampi showing a reduction of $Kv_{2.1}$ clusters' density in $Lgi1^{-/-}$. (Density of Clusters (#/µm$^3$) WT = 0.036 ± 0.002 $Lgi1^{-/-}$ = 0.020 ± 0.002; $p = 1.53 \times 10^{-6}$; Mann-Whitney *U* test; Surface of clusters (µm$^2$) WT = 3.48 ± 0.09 $Lgi1^{-/-}$ = 3.27 ± 0.08; $p = 0.08$; Two sample t-test; Normalized (to WT) immunoreactivity of clusters WT = 1.00 ± 0.01 $Lgi1^{-/-}$ = 0.99 ± 0.01; $p = 0.53$; Two sample *t*-test; Volume of clusters (µm$^3$) WT = 0.16 ± 0.01 $Lgi1^{-/-}$ = 0.15 ± 0.01; $p = 0.07$; Two sample t-test). **(F)** Representative 63× images showing a reduction of $Kv_{2.1}$ at the level of CA3 Pyr. neurons AIS (CA3 Str. Oriens) of $Lgi1^{-/-}$ hippocampus. Scale bar = 5 µm. **(G)** 63 Detail of a CA3 Pyr. neuron AIS in WT (top) and $Lgi1^{-/-}$ (bottom) showing a reduced density of $Kv_{2.1}$ clusters at the AIS of $Lgi1^{-/-}$ neurons. Scale bar = 2 µm. **(H)** Analysis of $Kv_{2.1}$ puncta in the AIS of CA3 pyramidal neurons in WT (black) and $Lgi1^{-/-}$ (red) showing a reduction of $Kv_{2.1}$ clusters' density and volume at the AIS of CA3 pyramidal neurons in $Lgi1^{-/-}$ mouse. (Density of Clusters (#/µm AIS) WT = 0.96 ± 0.03 $Lgi1^{-/-}$ = 0.69 ± 0.03; $p = 4.58 \times 10^{-7}$; Two sample *t*-test; Surface of clusters (µm$^2$) WT = 6.87 ± 0.41 $Lgi1^{-/-}$ = 5.85 ± 0.27; $p = 0.07$; Mann-Whitney U test; Normalized (to WT) immunoreactivity of clusters WT = 1.00 ± 0.02 $Lgi1^{-/-}$ = 0.96 ± 0.01; $p = 0.09$; Mann-Whitney U test; Volume of clusters (µm$^3$) WT = 0.23 ± 0.01 $Lgi1^{-/-}$ = 0.18 ± 0.01; $p = 0.046$; Mann-Whitney U test).

sequence homology with WD40 sequences (Yamagata et al., 2018) and may reflect a particular propensity of Kv1 subunits to associate with some WD40 motif-containing proteins. This finding supports the suggested changes in the phosphorylation-mediated dynamic balance and stability of $Kv_1$ membrane expression in *Lgi1*$^{-/-}$ (Connors et al., 2008). In parallel to the acquired association with endocytotic markers, the association of $Kv_1$ with syntaxin1B was also increased.

### 3.4. *Kv$_2$ expression is decreased in Lgi1*$^{-/-}$

Homo-tetrameric $Kv_2$ delayed-rectifier potassium channels are widely expressed though hetero-oligomers can occur in some cells (Bishop et al., 2015). VAPA/B interact with $Kv_{2.1}$ and $Kv_{2.2}$ channel subunits (Johnson et al., 2018) and induce the formation of channel clusters (Bishop et al., 2015). At PM/ER contact sites, $Kv_2$ clusters constitute trafficking hubs where membrane protein insertion and retrieval take place (Johnson et al., 2019). As we observed an increase of VAPA association with $Kv_1$ in *Lgi1*$^{-/-}$ and a loss of $Kv_1$ association with the VAPA interaction partner ASTRA, we undertook to investigate whether $Kv_2$ expression in *Lgi1*$^{-/-}$ was modified. As shown in Fig. 5a and b, $Kv_{2.1}$ expression was specifically and drastically reduced in hippocampus ($Kv_{2.1}$ WT 1.00 ± 0.05 vs $Kv_{2.1}$ *Lgi1*$^{-/-}$ 0.45 ± 0.04, $p = 1.00 \times 10^{-9}$) compared to total brain homogenates ($Kv_{2.1}$ WT 1.00 ± 0.09 vs $Kv_{2.1}$ *Lgi1*$^{-/-}$ 1.01 ± 0.12, $p = 0.97$) where no difference was observed. $Kv_2$ channels provide a major component of somatodendritic potassium currents and occur at the neuronal surface either in conducting freely-diffusing forms or non-conducting clusters (Misonou et al., 2005). These channels are involved in the dynamic modulation of excitability during periods of high neuronal activity (Misonou et al., 2005) (Du et al., 2000). In addition, a decrease in $Kv_{2.1}$ expression leads to an increase in the propensity of neurons to exhibit complex spike bursting (Raus Balind et al., 2019). In order to get more insight into a potential modification in the expression of $Kv_{2.1}$ in the *Lgi1*$^{-/-}$ hippocampal formation, we performed immunohistochemical staining of $Kv_{2.1}$ in hippocampal slices. As described earlier (Palacio et al., 2017), $Kv_{2.1}$ was mostly enriched in the CA1 compared to the CA3 (Fig. 5C). We found that in *Lgi1*$^{-/-}$, the expression level of $Kv_{2.1}$ in the CA3 was severely decreased (Fig. 5C, E). A closer look at the distribution of this channel in the CA3 showed also considerably reduced expression in the stratum oriens (SO) and stratum pyramidale (SP) (Fig. 5D, F) and that AIS labelling was severely diminished (Fig. 5F-H). We further analysed the following four distinct staining parameters, either in global staining or at the AIS: i) cluster density, ii) normalized immunoreactivity of the clusters, iii) cluster surface, and iv) cluster volume. As shown in Fig. 5E and Fig. 5H, cluster density was the only staining parameter that showed significant decrease in the global analysis or at the AIS. This fully converges with the previously reported dispersion of $Kv_{2.1}$ clusters in response to increased neuronal activity (Misonou et al., 2004) (Romer et al., 2016).

### 3.5. *Functional correlate of changes in Kv$_1$ & Kv$_2$ expression levels and interactome changes*

LGI1 is particularly enriched in the CA3 hippocampal subregions (Herranz-Perez et al., 2010) (Smedfors et al., 2018) (Ramirez-Franco et al., 2022) and plays a crucial role in regulating CA3 pyramidal neurons excitability (Seagar et al., 2017) (Kornau et al., 2020) (Extremet et al., 2022). Moreover, focal CA3 hippocampal atrophy is observed in autoimmune LGI1-mediated limbic encephalitis (Miller et al., 2017). It has also been pointed out that a decrease in somatodendritic D-type potassium currents (Metz et al., 2007) (Golding et al., 1999) (Golding et al., 2001) (Hyun et al., 2015) (Eom et al., 2019) and a weak expression of $Kv_2$ channels (Raus Balind et al., 2019) could promote the appearance of bursting patterns in hippocampal neurons. In order to examine LGI1 deficiency-mediated modification in excitability independently from potential artefacts induced by slice culture conditions, we examined intrinsic excitability of CA3 pyramidal neurons from acute slices. To examine changes in excitability at the CA3 hippocampal level, we performed current clamp recordings from CA3 pyramidal neurons of WT and their *Lgi1*$^{-/-}$ littermates (Fig. 6A, B). Similar to organotypic slices, we observed a marked increase of the excitability in CA3 pyramidal neurons from *Lgi1*$^{-/-}$ defined by a pronounced decrease in the rheobase (WT = 119 ± 20 pA vs *Lgi1*$^{-/-}$ = 45 ± 4 pA; $p = 5 \times 10^{-6}$, Mann-Whitney U test) and a significant reduction of the latency to the first spike at the rheobase current (WT = 482 ± 40 ms vs. *Lgi1*$^{-/-}$ = 341 ± 30 ms; $p = 0.007$, Mann-Whitney U test) (Fig. 6C, D, E). Neither the AP half-width (WT = 1.22 ± 0.02 ms vs. *Lgi1*$^{-/-}$ = 1.20 ± 0.02 ms; $p = 0.55$, Two samples t-test), nor amplitude (WT = 90.10 ± 0.93 mV vs. *Lgi1*$^{-/-}$ = 92.61 ± 1.00 mV; p = 0.07, Two samples t-test) were modified (Fig. 6F-H). This is consistent with previous observations showing that the broadening of AP due to the loss or pharmacological inhibition of $Kv_{1.1}$ is only noticeable in presynaptic but not in somatic APs (Vivekananda et al., 2017). Interestingly, we observed a proportion of CA3 pyramidal neurons that exhibit spike bursts at the rheobase (Fig. 6I, J). Although this kind of firing pattern has been previously described (Masukawa et al., 1982) (Raus Balind et al., 2019) in WT cells, the proportion of neurons exhibiting bursts was substantially larger in *Lgi1*$^{-/-}$ mice compared to their WT littermates ($WT_{bursting\ cells}$ = 6.67%, [2/30 cells] vs. *Lgi1*$^{-/-}$ $_{bursting\ cells}$ = 48.57%, [17/35 cells]; $p = 0.0003$ Fisher's exact test) (Fig. 6K, L). In order to address bursting propensity and based on previous work that focused on this type of firing pattern in CA3 pyramidal neurons (Raus Balind et al., 2019), we performed a different set of experiments in which neurons were challenged with either 300 pA or 600 pA current injection pulses (0.5 ms). The proportion of cells bursting at 300pA was significantly larger in *Lgi1*$^{-/-}$ mice (WT = 12.5% [1/8 cells] vs. *Lgi1*$^{-/-}$ 87.5% [7/8 cells]; $p = 0.01$ Fisher's exact test) and virtually all the *Lgi1*$^{-/-}$ cells challenged with 600 pA current injections exhibited a bursting pattern (WT = 12.5% [1/8 cells] vs. *Lgi1*$^{-/-}$ 100% [8/8 cells]; $p = 0.001$ Fisher's exact test) (Fig. 6M-O).

## 4. Discussion

In this study we combined immunofluorescence and mass spectrometry experiments to address modifications in $Kv_1$ distribution and interactome in *Lgi1*$^{-/-}$. It was previously reported that $Kv_1$ channels undergo a severe downregulation in mice lacking LGI1 (Seagar et al., 2017), as well as upon in vivo hippocampal infusion of LGI1 antibodies (Petit-Pedrol et al., 2018). In this study, we performed a detailed immunohistochemical analysis of $Kv_{1.1}$ and $Kv_{1.2}$ expression at the *Lgi1*$^{-/-}$ hippocampus. The use of antigen retrieval techniques, a necessary condition to reveal $Kv_1$ immunoreactivity at the AIS of hippocampal neurons (Lorincz and Nusser, 2008a), allowed an accurate and reliable analysis of modifications of the $Kv_1$ expression pattern at the cellular and subcellular levels. To our knowledge, this is the first time that $Kv_1$ expression at the AIS has been evaluated in fixed brains of *Lgi1*$^{-/-}$ mice. In addition to previous observations on $Kv_1$ downregulation at the AIS, we uncovered an important overall decrease in all neuronal compartments. This finding reflects more adequately the massive decrease in $Kv_1$ expression measured in Western blots since the reduction of $Kv_1$ population in the AIS cannot account for the >50% overall decrease. The relatively stable expression of $Kv_{1.1}$ and $Kv_{1.2}$ in PV+ interneurons is consistent with the finding that the electrophysiological properties of PV interneurons were unchanged in *Lgi1*$^{-/-}$ (Zhou et al., 2018), and that deleting LGI1 in PV+ interneurons did not influence seizure susceptibility (Boillot et al., 2014).

Our results indicate that, the antibody that we used for immunoprecipitation and mass spectrometry analysis can cross react, but only with closely related and significantly homologous $Kv_1$ family members. The absence of recognition of $Kv_{1.1}$ expressed in HEK cells may be due to the limited expression level of recombinant channels in eukaryotic cells. Mass spectrometry analysis of $Kv_1$-associated complexes in *Lgi1*$^{-/-}$ revealed intricate molecular changes in the $Kv_1$ interactome. The

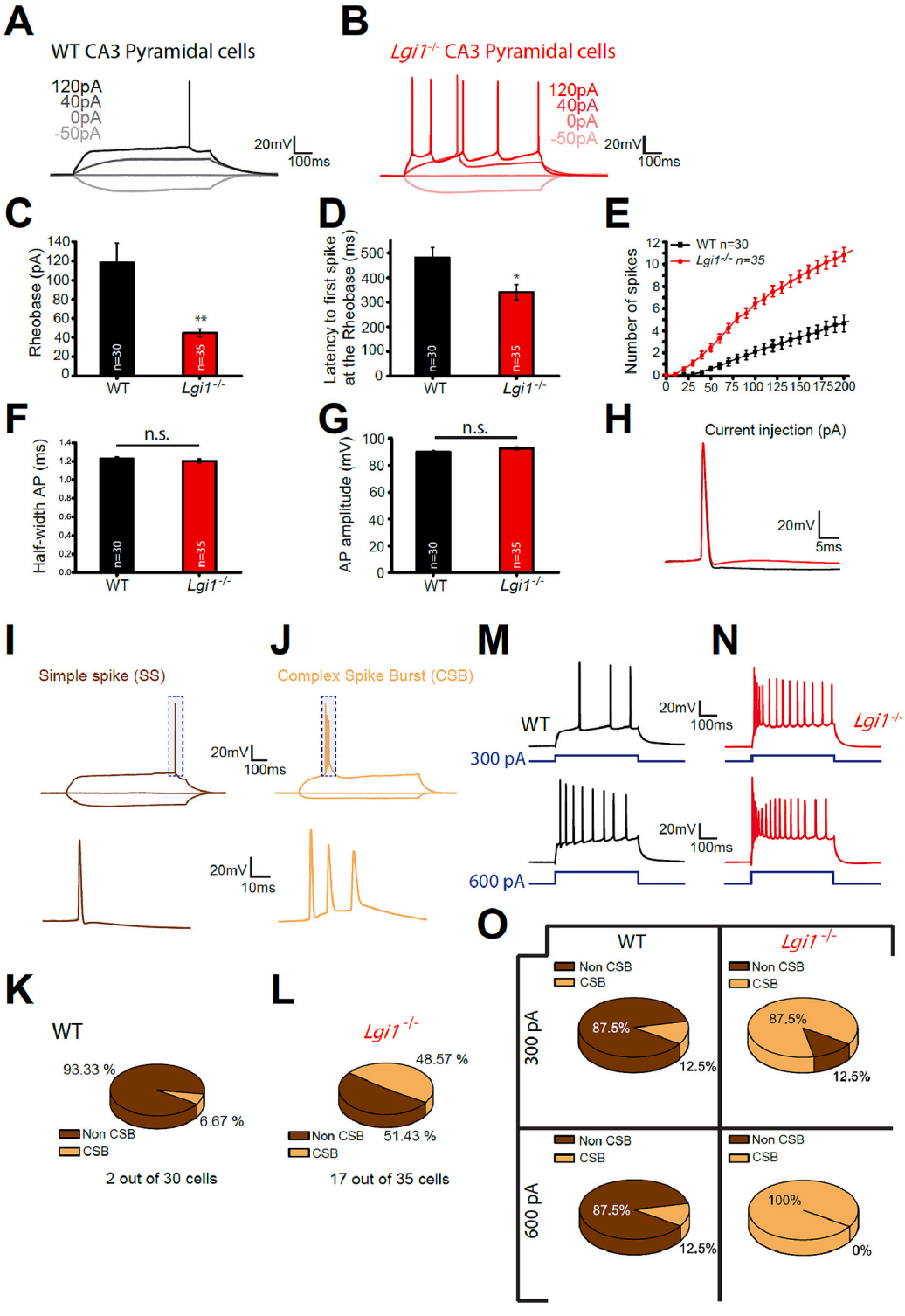


*(caption on next page)*

**Fig. 6.** Intrinsic excitability and bursting propensity are increased in *Lgi1*$^{-/-}$ CA3 Pyramidal neurons.
**(A)** representative traces for WT CA3 pyramidal neurons in response to the indicated current injections. **(B)** representative traces for *Lgi1*$^{-/-}$ CA3 pyramidal neurons in response to the indicated current injections. **(C)** Average rheobase values for WT (black) and *Lgi1*$^{-/-}$ (red) CA3 pyramidal neurons (WT = 116.00 ± 19.35 pA *Lgi1*$^{-/-}$ = 44.86 ± 4.00 pA; p = 0.001; Two sample t-test). **(D)** Average latency values to the first spike at the rheobase in WT (black) and *Lgi1*$^{-/-}$ (red) CA3 pyramidal neurons (WT = 475.60 ± 39.33 ms *Lgi1*$^{-/-}$ = 341.40 ± 29.83 ms; p = 0.007; Two sample t-test). **(E)** Average input-output curves of WT (black) and *Lgi1*$^{-/-}$ (red) CA3 pyramidal neurons. **(F)** Half-width of action potentials in WT (black) and *Lgi1*$^{-/-}$ (red) CA3 pyramidal neurons (WT = 1.22 ± 0.02 ms *Lgi1*$^{-/-}$ = 1.20 ± 0.02 ms; p = 0.55; Two sample t-test). **(G)** Amplitude of action potentials in WT (black) and *Lgi1*$^{-/-}$ (red) CA3 pyramidal neurons (WT = 90.09 ± 0.93 mV *Lgi1*$^{-/-}$ = 92.61 ± 1.00 mV; p = 0.07; Two sample t-test). **(H)** representative traces in current-clamp recordings showing the shape of an AP in WT (black) and *Lgi1*$^{-/-}$ (red) CA3 Pyramidal neurons. **(I)** Non-complex spike bursts (single AP, dark brown) and **(J)** Complex-spike burst (light brown) recorded in current clamp in CA3 pyramidal neurons. **(K)** proportion of CSB and Non-CSB neurons at the rheobase in WT CA3 pyramidal neurons. **(L)** Proportion of CSB and Non-CSB neurons at the rheobase in *Lgi1*$^{-/-}$ CA3 pyramidal neurons. **(M)** Representative traces of bursting propensity in WT CA3 pyramidal neurons studied by suprathreshold current injections at 300 pA (top) and 600 pA (bottom) respectively. **(N)** Representative traces of bursting propensity in *Lgi1*$^{-/-}$ CA3 pyramidal neurons studied by suprathreshold current injections at 300 pA (top) and 600 pA (bottom) respectively. **(O)** The proportion of CA3 pyramidal cells exhibiting a bursting phenotype is increased in the *Lgi1*$^{-/-}$ mouse (at 300 pA CSB WT = 12.5% [1/8 cells] vs. CSB *Lgi1*$^{-/-}$ 87.5% [7/8 cells]; p = 0.01 Fisher's exact test; at 600 pA CSB WT = 12.5% [1/8 cells] vs. CSB *Lgi1*$^{-/-}$ 100% [8/8 cells]; *p = 0.001* Fisher's exact test). For panels A to L WT *n* = 30 cells from 8 animals; KO *n* = 35 cells from 8 animals. For panels M to O WT *n* = 8 cells from 2 animals; KO n = 8 cells from 4 animals.

comparison between Kv1 partners in WT and *Lgi1*$^{-/-}$ uncovered intriguing findings, suggesting a dynamic interplay of protein interactions. Certain partners were lost in the absence of LGI1, while new partners were acquired, highlighting the remodelling of $Kv_1$ interaction networks. The most striking reorganisation is the loss of Kv1 interaction with several cytoskeletal elements. These data are corroborated by a previously published study showing an increased detergent solubility of $Kv_1$ channel in *Lgi1*$^{-/-}$ (Fukata et al., 2010). Besides the major impact on the Kv1 association with the cytoskeletal network, the -significant modification in $Kv_1$ association with 14–3-3 proteins may be an important readout of the perturbations associated with the absence of LGI1. 14–3-3 are homo /hetero multimeric cytosolic phosphoproteins that are highly expressed in brain and implicated in cell signalling pathways. 14–3-3γ mutations have been shown to be associated with several brain disorders such as epileptic encephalopathy (Allen et al., 2013) (Guella et al., 2017) as well as febrile seizures (Ye et al., 2021). Also, 14–3-3γ plays a pivotal role in oligodendrocytic apoptosis and neuroinflammation (Lee et al., 2015). Recently, it was shown that ADAM22 phosphorylation ($S_{832}$) stabilizes its interaction with 14–3-3 proteins (ε, ξ, θ, γ, β, and η) and protects it from endocytosis (Yokoi et al., 2021). Of note, the loss of interaction of 14–3-3 with non-phosphorylated ADAM22 does not influence ADAM22 association with LGI1, $Kv_{1.2}$ or PSD95. It is therefore tempting to speculate that in *Lgi1*$^{-/-}$ mice, a homeostatic neuronal response aiming at stabilizing membrane $Kv_1$ drives an increase in ADAM22 / 14–3-3 / $Kv_{1.2}$ association. Further investigation of the $Kv_1$ phospho-proteome is still necessary to explore these suggestions. The absence of ADAM23 association with Kv1 in wild type samples is surprising in the light of the current view of the literature placing ADAM23 as a presynaptic organizer of Kv1 channels. Previous immunoprecipitations using anti-C-terminal $Kv_{1.2}$ antibodies also did not show association with ADAM23 (Ogawa et al., 2010). Whether the absence of ADAM23 is the result of epitope accessibility in $Kv_1$ / ADAM23 complexes or reflects a real molecular organisation is still to be addressed.

An additional important perturbation was the sharp reduction in the expression level of PSD93 in whole-brain and hippocampal homogenates, with a prominent reduction at the AIS of CA3 pyramidal neurons. Although PSD93 is one of the major constituents of LGI1 (Fukata et al., 2010) (Hossen et al., 2022) and ADAM22-associated complexes (Fukata et al., 2021), it is weakly associated with $Kv_{1.2}$ in whole brain extracts (Ogawa et al., 2010). The observed specific loss of interaction with PSD93 is consistent with the previously published data showing that PSD93 but not PSD95 (Rasband et al., 2002) (Ogawa et al., 2010) nor ADAM22 (Ogawa et al., 2010), is important in $Kv_{1.1}$ and $Kv_{1.2}$ channel localisation and clustering at AIS (Ogawa et al., 2008). The selective decrease in PSD93 expression contrasts with the reported stability of PSD95 expression level in the *Lgi1*$^{-/-}$ background (Lovero et al., 2015) and shows that the association of $Kv_1$ with PSD93 is dependent on the presence of LGI1. Interestingly, RhoA activity has been shown to be significantly increased in *Lgi1*$^{-/-}$ (Thomas et al., 2018). Also, RhoA activity mediates spine morphological and functional plasticity (Kasai et al., 2021) (Woolfrey and Srivastava, 2016) and may therefore be linked to the observed actin cytoskeleton remodelling. Interestingly, PSD93 phosphorylation by RhoA was recently shown to decrease its binding to ADAM22 and to increase PSD93 heterodimerization with PSD95 (Hossen et al., 2022). The only partner of $Kv_1$ that interacts with PSD95/PSD93 and that is specifically lost in our immunoprecipitations from *Lgi1*$^{-/-}$ tissue is the plasma membrane calcium-transporting ATPase 4 (AT2B4 / PMCA4), that was shown to be enriched in lipid-rafts (Sepulveda et al., 2006). AT2B4 interaction with PSD95/93 has been shown to increase with neuronal excitability and glutamate release (Lisek et al., 2017). This increase in excitability leads to the activation of NMDA receptors and triggers AT2B4 selective internalization (Pottorf 2nd et al., 2006). In addition to these observations, it is known that the activity of AT2B4 is inhibited by 14–3-3ε (Rimessi et al., 2005) which interacts with and modulates the expression of the LGI1-binding partner ADAM22. Despite that the protein expression level of AT2B4 (PMCA4) did not show any significant difference between WT and *Lgi1*$^{-/-}$ samples (Supplementary Fig. S3), the loss of PSD93 co-immunoprecipitation with $Kv_1$ in *Lgi1*$^{-/-}$ may partially reflect the loss of $Kv_1$ association with AT2B4. Since LGI1 was shown to regulate PSD95-mediated AMPA and NMDA receptor levels in neurons (Lovero et al., 2015), it may be suggested that, in the *Lgi1*$^{-/-}$ epileptic model, a hyperexcitability-driven increase of interaction between PSD95 and AT2B4 could be blocked by the expected increase in RhoA-mediated PSD95/PSD93 interaction. Of note, it was recently reported that the truncation of the MAGUK binding domain of ADAM22 induces a massive reduction in hippocampal PSD95 expression levels (Fukata et al., 2021). In line with these observations, the loss of PSD93 co-immunoprecipitation with $Kv_1$ in *Lgi1*$^{-/-}$ may be the result of a RhoA-kinase phosphorylation of PSD93 and a concomitant delocalization of the PSD95/PSD93 complex. Further analysis is still necessary to understand the specificity of the seemingly key disruption of PSD93 association with $Kv_1$ complexes in *Lgi1*$^{-/-}$.

The most abundant partner of $Kv_1$ found in *Lgi1*$^{-/-}$ is the glyceraldehyde-3-phosphate dehydrogenase (G3P) (Supplementary Table S3, Supplementary Fig. S4) which is found with an emPAI (1.64 ± 0.34) close to the emPAI value of actin (2.12 ± 0.0) in wild type tissue (Supplementary Table S2, Supplementary Fig. S4). G3P is a moon-lighting protein involved in several regulatory pathways including synaptic transmission and intermembrane trafficking (Sirover, 2021). The second most abundant acquired interaction partner is the fatty-acid binding protein FABP7 which is involved in the uptake of fatty acids and serves as a cellular chaperone of lipophilic molecules. This protein is expressed in astrocytes and oligodendrocyte progenitor cells (OPCs) (Sharifi et al., 2011) (Sharifi et al., 2013) and has been shown to regulate dendritic morphology and excitatory synaptic function of cortical neurons (Ebrahimi et al., 2016).This observation is in line with the potential expression of $Kv_{1.2}$ in astrocytes (Akhtar et al., 1999). Interestingly,

among the newly acquired partners we found PCMD2 (protein-L-isoaspartate *O*-methyltransferase domain-containing protein 2) a member of the L-isoaspartyl *O*-methyltransferases (PIMT) protein family, known to repair natural protein damage (Kim et al., 1997) (Yamamoto et al., 1998) (Reissner et al., 2006) (Zhu et al., 2006). The presence of this protein in $Kv_1$-associated complexes may suggest that at least some of its components may be under repair and imply a higher level of protein damage/recycling than in WT tissue. The presence of synapsin 2 (SYN2) and the voltage-dependent anion-selective channel protein 1 (VDAC1) in the $Kv_1$ interactome of *Lgi1*$^{-/-}$ corroborates this hypothesis since these proteins have been identified as major endogenous substrates for PIMT (Zhu et al., 2006). The association with the ATPase-dependent chaperone T-complex protein 1 subunit delta (TCPD) is in line with this interpretation and may highlight attempts for recovery from damage. This protein localises to dendrites where it is involved in microtubule organisation (Wang et al., 2020).

Trafficking pathways associated with $Kv_1$ also seem to have been affected in *Lgi1*$^{-/-}$ tissue, as the presence of AP1- and AP3-associated coat protein PACS1 decreased by >29% and the association with PSD1 (Cytohesin 1), a guanine nucleotide exchange factor for ARF6 involved in neuron projection development, protein trafficking and cytoskeletal rearrangements (Toma-Fukai and Shimizu, 2019), decreased by >38%. The acquisition of Kv1 association with VAMP2, syntaxin1A, synaptogyrin 3, copine1, synapsin as well as dynamin 3 (DYN3) indicate the presence of $Kv_1$ in vesicular compartments and suggest an increase in channel endocytosis. This is corroborated by the fact that neuronal activity blockade was shown to induce synaptic clustering of post-synaptic DYN3 (Calabrese and Halpain, 2015) (Gray et al., 2003) (Gray et al., 2005) and that TTX-induced neuronal activity blockade led to a reduction of the Kv1-mediated DTX-I sensitive current (Cudmore et al., 2010). Also, it has been shown that activity-dependent $Kv_{1.2}$ endocytosis in distal apical dendrites is mediated by DYN3 in CA3 pyramidal neurons (Hyun et al., 2013). Therefore, the acquirement of DYN3 association with $Kv_1$ may be the read out of this mechanism. Since Kv1 levels are reduced in *Lgi1*$^{-/-}$, the association of $Kv_1$ with DYN3 might reflect a mechanism of $Kv_1$ retrieval at the dendritic level. This hypothesis is corroborated by the acquired $Kv_1$ association in *Lgi1*$^{-/-}$ with annexin A2 (ANXA2), which is a membrane-associated pleiotropic calcium-dependent phospholipid binding protein involved in several aspects of cell biology related to calcium signalling and endocytosis. ANXA2 is enriched in lipid rafts (Zhao et al., 2004) and its secretion is activity-dependent (Zhao and Lu, 2007). It has been shown to be primarily present in GABAergic interneurons (Zhao and Lu, 2007) and is overexpressed in pathological neuronal and glial reactions (Eberhard et al., 1994). Therefore, its presence in the $Kv_1$ interactome in an *Lgi1*$^{-/-}$ background may be linked to the observed astrogliosis in these animals.

In addition to the perturbation of $Kv_1$ cytoskeletal links, $Kv_1$ transit from ER/Golgi to plasma membranes seems also to be affected since the association of $Kv_1$ with the Golgi adaptors AP3S1 and AP1B1 (Nakatsu et al., 2014) is disrupted. These adaptor proteins are known to play a crucial role in sorting the cargo destined ~~to~~ for plasma membranes, neurites and nerve terminals (Larimore et al., 2011) (Clemens Grisham et al., 2013).

An ER population of $Kv_1$ seems to be particularly prominent in *Lgi1*$^{-/-}$ samples. This conclusion is driven by the fact that in *Lgi1*$^{-/-}$, $Kv_1$ is associated with LRRC59 and RPN1. LRRC59 is an ER mRNA receptor known to participate in coupling translation and ER membrane insertion of transmembrane-domain containing proteins (Bhadra et al., 2021) and RPN1 (dolichyl-diphosphooligosaccharide-protein glycosyltransferase subunit 1 is involved in early glycosylation steps of nascent proteins. The association with the receptor of activated protein C kinase 1 (RACK1), PKCγ (KPCG), the cAMP-dependent protein kinase catalytic subunit beta (KAPCB) and the adenylate cyclase activator LANC2 (Fresia et al., 2016) may reflect a change in phosphorylation-mediated dynamic balance and stability of $Kv_1$ membrane expression (Connors et al., 2008). Finally, the acquisition of association with L-lactate dehydrogenase B chain (LDHB) may indicate a functional modulation of channel activity since LDBH is part of the oxydoreductase complex and is involved in NAD metabolism which is important in $Kv_{1.2}$ activity modulation (Vacher and Trimmer, 2011). In parallel to this association, $Kv_1$ coimmunoprecipitated with the voltage-dependent anion-selective channel protein 1 (VDAC1) that binds sphingolipids, cholesterol and phosphatidylcholine and is involved in apoptosis and energy metabolism.

All these results underscore the complex nature of $Kv_1$ interactions, where the absence of LGI1 leads to an elaborate rewiring of protein partnerships, resulting in both gains and losses that intricately modulate the network dynamics and underly a complex deleterious phenotype in the *Lgi1*$^{-/-}$ mouse.

In parallel to the direct observations driven by mass spectrometry analysis, we report for the first time a massive hippocampal reduction in $Kv_2$ in *Lgi1*$^{-/-}$. Similar to AMPA receptors that are downregulated in *Lgi1*$^{-/-}$ but are not immonuprecipitated with LGI1 antibodies, $Kv_2$ is downregulated in *Lgi1*$^{-/-}$ but was not immunoprecipitated with $Kv_1$ antibodies. This suggests that in *Lgi1*$^{-/-}$, downregulation of AMPA receptors and $Kv_2$ channels may be the result of a complex molecular reorganisation in response to increased neuronal excitability. As a matter of fact, in *Lgi1*$^{-/-}$ the interaction of Kv1 with the F-actin-binding and phosphatase recruiter NEB2 is lost. This protein is a regulatory subunit of protein phosphatase 1 (Molina-Pinelo et al., 2011) that controls serine/threonine dephosphorylation of several membrane proteins such as ion channels and certain G-protein coupled receptors (Misonou et al., 2004) and is enriched in postsynaptic compartments (Satoh et al., 1998) where it is involved in modulating spine maturation and morphology (Wang et al., 2021). In accordance with this observation, PP2BB association with $Kv_1$ was lost in *Lgi1*$^{-/-}$. PP2BB is a regulatory subunit of the activity-dependent serine/threonine-protein phosphatase calcineurin and plays an essential role in intracellular $Ca^{2+}$-mediated signal transduction. With PP1, it plays a regulatory role in $Kv_{2.1}$ phosphorylation modulating its activity, membrane clustering and internalization with key effects on the control of neuronal excitability (Misonou et al., 2006) (Misonou et al., 2004). Interestingly, the interaction of NEB2 with actin is modulated by doublecortin (DCX) (Tsukada et al., 2005) and we found that this protein is acquired as a new partner of $Kv_1$ in *Lgi1*$^{-/-}$ samples. Also, the interaction with $Kv_1$ of the tether protein VAPA was massively upregulated in *Lgi1*$^{-/-}$. VAPA/B are $Kv_2$-interacting tether proteins located at membrane contact sites between the endoplasmic reticulum (ER) and the plasma membrane (PM) (James and Kehlenbach, 2021) which are rich in AKAPs, kinases, Rabs and non-vesicular lipid transfer proteins (i.e ASTRA, ASTRB (Ferrari et al., 2020)). VAPA/B possess a large number of common interactors, although, a specific interactome for each VAP does exist, it does not point to any clear functional difference between the two (James and Kehlenbach, 2021). The reason for the selective change in VAPA remains obscure, however, it may be related to the observed increase in the ER population of $Kv_1$ and suggests that LGI1 is involved in the presence of $Kv_1$ channels at ER/PM contact sites. Whether the increase in VAPA levels is linked to the increase in $Kv_1$ association with ER proteins needs further investigation.

In addition to the crucial role of $Kv_1$ channels in tuning the excitability of CA3 pyramidal neurons (Rama et al., 2017), its decrease at the somatodendritic compartment may trigger an increased after-depolarization (Metz et al., 2007). Moreover, the reduction in $Kv_2$ expression may trigger an increase in dendritic calcium spikes. These two different mechanisms could act synergistically facilitating bursting (Metz et al., 2007) (Raus Balind et al., 2019). Our results are also in agreement with other described forms of increased excitability in *Lgi1*$^{-/-}$ mice (Yu et al., 2010) (Zhou et al., 2018) (Boillot et al., 2016), and with the observed increase in excitability upon the treatment of slices with LGI1 antibodies (Lalic et al., 2011) (Kornau et al., 2020) (Extremet et al., 2022). The importance of $Kv_2$ downregulation in perturbing excitability in LGI1 deficiency is also highlighted by the fact that restoring $Kv_{1.1}$ expression in secretion-deficient LGI1$^{W183R}$ neurons does

not fully rescue the life span of mice (Zhou et al., 2023). Further investigations are needed to address whether LGI1 is directly implicated in modulating $Kv_2$ expression levels and whether $Kv_1$ downregulation is parallel to or consequent to $Kv_2$ downregulation.

In the light of the concomitant decrease in $Kv_1$ and $Kv_2$ expression levels, we addressed the intrinsic excitability of CA3 pyramidal neurons of *Lgi1*$^{-/-}$. We and others have previously shown that LGI1 is particularly enriched in CA3 hippocampal subregion (Herranz-Perez et al., 2010) (Smedfors et al., 2018) (Ramirez-Franco et al., 2022) and that LGI1 is crucial in controlling neuronal excitability in CA3 pyramidal neurons (Seagar et al., 2017) (Kornau et al., 2020) (Extremet et al., 2022). Moreover, LGI1 antibody-mediated limbic encephalitis is coincident with focal CA3 hippocampal atrophy in human patients (Miller et al., 2017). Although we have previously characterized the intrinsic excitability in pyramidal CA3 neurons of *Lgi1*$^{-/-}$ cultured hippocampal slices (Seagar et al., 2017), it has been proposed that cultured hippocampal slices spontaneously develop epileptiform activity (Dyhrfjeld-Johnsen et al., 2010). To eliminate a potential bias introduced by the use of organotypic cultures, and to gain further understanding of the mechanisms underlying LGI1 deficiency-mediated epilepsy, we analysed intrinsic excitability of CA3 pyramidal neurons from acute slices.

We observed an increase in neuronal burst firing propensity and intrinsic excitability defined as a decrease in the rheobase and a shortened latency to the first spike. This gain in excitability converges with the decrease in $Kv_{1.1}$ and $Kv_{1.2}$ as well as $Kv_2$ described throughout this study, and is in accordance with the crucial role of $Kv_1$ channels in tuning CA3 pyramidal neurons excitability (Rama et al., 2017) and the implication of dendritic D-type potassium currents (Metz et al., 2007) and $Kv_2$ channels (Raus Balind et al., 2019) in promoting bursting patterns in hippocampal neurons. Our results are also in agreement with other described forms of increased excitability in *Lgi1*$^{-/-}$ mice (Yu et al., 2010) (Zhou et al., 2023) (Boillot et al., 2016), and with the observed increase in excitability upon the treatment of slices with LGI1 antibodies (Lalic et al., 2011) (Kornau et al., 2020) (Extremet et al., 2022). As expectedly, there was no change in AP waveform since the broadening of the AP due to the loss or pharmacological inhibition of $Kv_{1.1}$ is only noticeable in presynaptic, but not in somatic APs (Vivekananda et al., 2017).

Although these promising results deserve further investigation, it is widely accepted that synchronized bursting is the cellular substrate for interictal spikes, which, in turn, constitute a hallmark of epilepsy (Traub and Wong, 1982) (Xu and Clancy, 2008). Given the high degree of recurrent connectivity in the CA3 hippocampal region (Mitra et al., 2011) (Guzman et al., 2016), it is tempting to propose a cellular landscape in which the abnormally increased burst firing, in combination with a lower firing threshold in *Lgi1*$^{-/-}$ CA3 pyramidal neurons, triggers the epileptogenic phenotype observed in *Lgi1*$^{-/-}$ mice.

## CRediT authorship contribution statement

**Jorge Ramirez-Franco:** Validation, Methodology, Investigation, Formal analysis, Data curation, Conceptualization, Visualization, Writing – original draft, Writing – review & editing. **Kévin Debreux:** Data curation, Investigation. **Marion Sangiardi:** Investigation, Methodology. **Maya Belghazi:** Data curation, Investigation, Writing – original draft. **Yujin Kim:** Resources. **Suk-Ho Lee:** Resources. **Christian Lévèque:** Conceptualization, Validation, Writing – original draft, Writing – review & editing. **Michael Seagar:** Conceptualization, Writing – original draft, Writing – review & editing. **Oussama El Far:** Conceptualization, Data curation, Formal analysis, Funding acquisition, Investigation, Methodology, Project administration, Supervision, Validation, Visualization, Writing – original draft, Writing – review & editing.

## Declaration of competing interest

The authors declare that they have no conflict of interest.

## Data availability

All data needed to evaluate the conclusions in the paper are present in the paper and/or the Supplementary Materials. The proteomic data were deposited on the PRIDE website (https://www.ebi.ac.uk/pride/archive) with the dataset identifier PXD043649.

## Acknowledgements

We thank Stephanie Baulac for sharing the *Lgi1*$^{-/-}$ mice strain (Chabrol et al., 2010) and Jeffrey Martens (University of Michigan, USA) for providing Kv1 clones (Jenkins et al., 2011). This work was supported by the Institut National de la Santé et de la Recherche Médicale INSERM), Aix-Marseille Université (AMU) and the Agence Nationale de la Recherche (ANR) (grant ANR-17-CE16-0022). The postdoctoral financial support of J.R.F. was from the ANR (grant ANR-17-CE16-0022). The PhD thesis by K.D. was supported by a fellowship from the French Ministry of Research (MESRI).

## Appendix A. Supplementary data

Supplementary data to this article can be found online at https://doi.org/10.1016/j.nbd.2024.106513.

## References

Akhtar, S., et al., 1999. A functional spliced-variant of beta 2 subunit of Kv1 channels in C6 glioma cells and reactive astrocytes from rat lesioned cerebellum. Biochemistry 38, 16984–16992.
Allen, A.S., et al., 2013. De novo mutations in epileptic encephalopathies. Nature 501, 217–221.
Bhadra, P., et al., 2021. Quantitative proteomics and differential protein abundance analysis after depletion of putative mRNA receptors in the ER membrane of human cells identifies novel aspects of mRNA targeting to the ER. Molecules 26.
Bishop, H.I., et al., 2015. Distinct cell- and layer-specific expression patterns and independent regulation of Kv2 channel subtypes in cortical pyramidal neurons. J. Neurosci. 35, 14922–14942.
Boillot, M., et al., 2014. Glutamatergic neuron-targeted loss of LGI1 epilepsy gene results in seizures. Brain : J. Neurol. 137, 2984–2996.
Boillot, M., et al., 2016. LGI1 acts presynaptically to regulate excitatory synaptic transmission during early postnatal development. Sci. Rep. 6, 21769.
Bolte, S., Cordelieres, F.P., 2006. A guided tour into subcellular colocalization analysis in light microscopy. J. Microsc. 224, 213–232.
Browne, D.L., et al., 1994. Episodic ataxia/myokymia syndrome is associated with point mutations in the human potassium channel gene, KCNA1. Nat. Genet. 8, 136–140.
Calabrese, B., Halpain, S., 2015. Differential targeting of dynamin-1 and dynamin-3 to nerve terminals during chronic suppression of neuronal activity. Mol. Cell. Neurosci. 68, 36–45.
Chabrol, E., et al., 2010. Electroclinical characterization of epileptic seizures in leucine-rich, glioma-inactivated 1-deficient mice. Brain : J. Neurol. 133, 2749–2762.
Chen, B., et al., 2014. The WAVE regulatory complex links diverse receptors to the actin cytoskeleton. Cell 156, 195–207.
Cho, S.J., et al., 2011. Septin 6 regulates the cytoarchitecture of neurons through localization at dendritic branch points and bases of protrusions. Mol. Cell 32, 89–98.
Clemens Grisham, R., et al., 2013. Mutations in ap1b1 cause mistargeting of the Na(+)/K(+)-ATPase pump in sensory hair cells. PLoS One 8, e60866.
Connors, E.C., et al., 2008. Homeostatic regulation of Kv1.2 potassium channel trafficking by cyclic AMP. J. Biol. Chem. 283, 3445–3453.
Cudmore, R.H., et al., 2010. Spike-time precision and network synchrony are controlled by the homeostatic regulation of the D-type potassium current. J. Neurosci. 30, 12885–12895.
Debanne, D., et al., 2011. Axon physiology. Physiol. Rev. 91, 555–602.
Di Giovanni, J., et al., 2010. V-ATPase membrane sector associates with synaptobrevin to modulate neurotransmitter release. Neuron 67, 268–279.
Ding, J., et al., 2016. Pore-forming activity and structural autoinhibition of the gasdermin family. Nature 535, 111–116.
Doring, J.H., et al., 2021. Refining genotypes and phenotypes in KCNA2-related neurological disorders. Int. J. Mol. Sci. 22.
Du, J., et al., 2000. Frequency-dependent regulation of rat hippocampal somato-dendritic excitability by the K+ channel subunit Kv2.1. J. Physiol. 522 Pt 1, 19–31.
Dyhrfjeld-Johnsen, J., et al., 2010. Interictal spikes precede ictal discharges in an organotypic hippocampal slice culture model of epileptogenesis. J. Clin. Neurophysiolo. : Off. Publicat. American Electroencephalograph. Soc. 27, 418–424.
Eberhard, D.A., et al., 1994. Alterations of annexin expression in pathological neuronal and glial reactions. Immunohistochemical localization of annexins I, II (p36 and p11 subunits), IV, and VI in the human hippocampus. Am. J. Pathol. 145, 640–649.
Ebrahimi, M., et al., 2016. Astrocyte-expressed FABP7 regulates dendritic morphology and excitatory synaptic function of cortical neurons. Glia 64, 48–62.

Eom, K., et al., 2019. Intracellular Zn(2+) signaling facilitates mossy Fiber input-induced Heterosynaptic potentiation of direct cortical inputs in hippocampal CA3 pyramidal cells. J. Neurosci. 39, 3812–3831.
Extremet, J., et al., 2022. An epitope-specific LGI1-autoantibody enhances neuronal excitability by modulating Kv1.1 channel. Cells 11.
Extremet, J., et al., 2023. Rescue of Normal Excitability in LGI1-deficient epileptic neurons. J. Neurosci. 43, 8596–8606.
Ferrari, A., et al., 2020. Aster proteins regulate the accessible cholesterol Pool in the plasma membrane. Mol. Cell. Biol. 40.
Flores, A., et al., 2019. Gangliosides interact with synaptotagmin to form the high-affinity receptor complex for botulinum neurotoxin B. Proc. Natl. Acad. Sci. USA 116, 18098–18108.
Fresia, C., et al., 2016. G-protein coupling and nuclear translocation of the human abscisic acid receptor LANCL2. Sci. Rep. 6, 26658.
Fukata, Y., et al., 2006. Epilepsy-related ligand/receptor complex LGI1 and ADAM22 regulate synaptic transmission. Science 313, 1792–1795.
Fukata, Y., et al., 2010. Disruption of LGI1-linked synaptic complex causes abnormal synaptic transmission and epilepsy. Proc. Natl. Acad. Sci. USA 107, 3799–3804.
Fukata, Y., et al., 2021. LGI1-ADAM22-MAGUK configures transsynaptic nanoalignment for synaptic transmission and epilepsy prevention. In: Proceedings of the National Academy of Sciences of the United States of America, 118.
Golding, N.L., et al., 1999. Dendritic calcium spike initiation and repolarization are controlled by distinct potassium channel subtypes in CA1 pyramidal neurons. J. Neurosci. 19, 8789–8798.
Golding, N.L., et al., 2001. Dichotomy of action-potential backpropagation in CA1 pyramidal neuron dendrites. J. Neurophysiol. 86, 2998–3010.
Gray, N.W., et al., 2003. Dynamin 3 is a component of the postsynapse, where it interacts with mGluR5 and Homer. Curre. Biol. : CB. 13, 510–515.
Gray, N.W., et al., 2005. A dynamin-3 spliced variant modulates the actin/cortactin-dependent morphogenesis of dendritic spines. J. Cell Sci. 118, 1279–1290.
Gu, C., et al., 2003. A conserved domain in axonal targeting of Kv1 (shaker) voltage-gated potassium channels. Science 301, 646–649.
Guella, I., et al., 2017. De novo mutations in YWHAG cause early-onset epilepsy. Am. J. Hum. Genet. 101, 300–310.
Guzman, S.J., et al., 2016. Synaptic mechanisms of pattern completion in the hippocampal CA3 network. Sciences 353, 1117–1123.
Haddjeri-Hopkins, A., et al., 2021. Refining the identity and role of Kv4 channels in mouse substantia Nigra dopaminergic neurons. eNeuro 8.
Herranz-Perez, V., et al., 2010. Regional distribution of the leucine-rich glioma inactivated (LGI) gene family transcripts in the adult mouse brain. Brain Res. 1307, 177–194.
Herson, P.S., et al., 2003. A mouse model of episodic ataxia type-1. Nat. Neurosci. 6, 378–383.
Hossen, E., et al., 2022. Rho-kinase/ROCK phosphorylates PSD-93 downstream of NMDARs to orchestrate synaptic plasticity. Int. J. Mol. Sci. 24.
Hyun, J.H., et al., 2013. Activity-dependent downregulation of D-type K+ channel subunit Kv1.2 in rat hippocampal CA3 pyramidal neurons. J. Physiol. 591, 5525–5540.
Hyun, J.H., et al., 2015. Kv1.2 mediates heterosynaptic modulation of direct cortical synaptic inputs in CA3 pyramidal cells. J. Physiol. 593, 3617–3643.
Inda, M.C., et al., 2006. Voltage-gated ion channels in the axon initial segment of human cortical pyramidal cells and their relationship with chandelier cells. Proc. Natl. Acad. Sci. USA 103, 2920–2925.
Irani, S.R., et al., 2010. Antibodies to Kv1 potassium channel-complex proteins leucine-rich, glioma inactivated 1 protein and contactin-associated protein-2 in limbic encephalitis, Morvan's syndrome and acquired neuromyotonia. Brain : J. Neurol. 133, 2734–2748.
James, C., Kehlenbach, R.H., 2021. The Interactome of the VAP family of proteins: an overview. Cells 10.
Jan, L.Y., Jan, Y.N., 2012. Voltage-gated potassium channels and the diversity of electrical signalling. J. Physiol. 590, 2591–2599.
Jenkins, P.M., et al., 2011. Subunit-dependent axonal trafficking of distinct alpha heteromeric potassium channel complexes. J. Neurosci. 31, 13224–13235.
Jiao, Y., et al., 1999. A simple and sensitive antigen retrieval method for free-floating and slide-mounted tissue sections. J. Neurosci. Methods 93, 149–162.
Johnson, B., et al., 2018. Kv2 potassium channels form endoplasmic reticulum/plasma membrane junctions via interaction with VAPA and VAPB. Proc. Natl. Acad. Sci. USA 115, E7331–E7340.
Johnson, B., et al., 2019. Kv2 channels create endoplasmic reticulum / plasma membrane junctions: a brief history of Kv2 channel subcellular localization. Channels 13, 88–101.
Johnston, J., et al., 2010. Going native: voltage-gated potassium channels controlling neuronal excitability. J. Physiol. 588, 3187–3200.
Kasai, H., et al., 2021. Spine dynamics in the brain, mental disorders and artificial neural networks. Nat. Rev. Neurosci. 22, 407–422.
Kim, E., et al., 1995. Clustering of shaker-type K+ channels by interaction with a family of membrane-associated guanylate kinases. Nature 378, 85–88.
Kim, E., et al., 1997. Deficiency of a protein-repair enzyme results in the accumulation of altered proteins, retardation of growth, and fatal seizures in mice. Proc. Natl. Acad. Sci. USA 94, 6132–6137.
Kornau, H.C., et al., 2020. Human cerebrospinal fluid monoclonal LGI1 autoantibodies increase neuronal excitability. Ann. Neurol. 87, 405–418.
Lalic, T., et al., 2011. Human limbic encephalitis serum enhances hippocampal mossy fiber-CA3 pyramidal cell synaptic transmission. Epilepsia 52, 121–131.
Larimore, J., et al., 2011. The schizophrenia susceptibility factor dysbindin and its associated complex sort cargoes from cell bodies to the synapse. Mol. Biol. Cell 22, 4854–4867.
Lee, D.H., et al., 2015. Role of glial 14-3-3 gamma protein in autoimmune demyelination. J. Neuroinflammation 12, 187.
Lee, Y., et al., 2020. Epilepsy- and intellectual disability-associated CYFIP2 interacts with both actin regulators and RNA-binding proteins in the neonatal mouse forebrain. Biochem. Biophys. Res. Commun. 529, 1–6.
Li, X., et al., 2009. Septin 11 is present in GABAergic synapses and plays a functional role in the cytoarchitecture of neurons and GABAergic synaptic connectivity. J. Biol. Chem. 284, 17253–17265.
Lisek, M., et al., 2017. Glutamate deregulation in ketamine-induced psychosis-a potential role of PSD95, NMDA receptor and PMCA interaction. Front. Cell. Neurosci. 11, 181.
Lorincz, A., Nusser, Z., 2008a. Cell-type-dependent molecular composition of the axon initial segment. J. Neurosci. 28, 14329–14340.
Lorincz, A., Nusser, Z., 2008b. Specificity of immunoreactions: the importance of testing specificity in each method. J. Neurosci. 28, 9083–9086.
Lovero, K.L., et al., 2015. The LGI1-ADAM22 protein complex directs synapse maturation through regulation of PSD-95 function. Proc. Natl. Acad. Sci. USA 112, E4129–E4137.
Magdaleno, S., et al., 2006. BGEM: an in situ hybridization database of gene expression in the embryonic and adult mouse nervous system. PLoS Biol. 4, e86.
Manigandan, S., Yun, J.W., 2022. Loss of cytoplasmic FMR1-interacting protein 2 (CYFIP2) induces browning in 3T3-L1 adipocytes via repression of GABA-BR and activation of mTORC1. J. Cell. Biochem. 123, 863–877.
Masukawa, L.M., et al., 1982. Variations in electrophysiological properties of hippocampal neurons in different subfields. Brain Res. 242, 341–344.
Metz, A.E., et al., 2007. Dendritic D-type potassium currents inhibit the spike afterdepolarization in rat hippocampal CA1 pyramidal neurons. J. Physiol. 581, 175–187.
Miller, T.D., et al., 2017. Focal CA3 hippocampal subfield atrophy following LGI1 VGKC-complex antibody limbic encephalitis. Brain : J. Neurol. 140, 1212–1219.
Misonou, H., et al., 2004. Regulation of ion channel localization and phosphorylation by neuronal activity. Nat. Neurosci. 7, 711–718.
Misonou, H., et al., 2005. Kv2.1: a voltage-gated k+ channel critical to dynamic control of neuronal excitability. Neurotoxicology 26, 743–752.
Misonou, H., et al., 2006. Bidirectional activity-dependent regulation of neuronal ion channel phosphorylation. J. Neurosci. 26, 13505–13514.
Mitra, A., et al., 2011. Heterogeneous reallocation of presynaptic efficacy in recurrent excitatory circuits adapting to inactivity. Nat. Neurosci. 15, 250–257.
Molina-Pinelo, S., et al., 2011. Down-regulation of spinophilin in lung tumours contributes to tumourigenesis. J. Pathol. 225, 73–82.
Murrin, L.C., Talbot, J.N., 2007. RanBPM, a scaffolding protein in the immune and nervous systems. J. Neuroimm. Pharmacol. : Off. J. Soc. NeuroImm. Pharmacol. 2, 290–295.
Nakatsu, F., et al., 2014. The role of the Clathrin adaptor AP-1: polarized sorting and beyond. Membranes 4, 747–763.
Neubauer, K., Zieger, B., 2017. The mammalian Septin Interactome. Front. Cell Development. Biol. 5, 3.
Ogawa, Y., et al., 2008. Postsynaptic density-93 clusters Kv1 channels at axon initial segments independently of Caspr2. J. Neurosci. 28, 5731–5739.
Ogawa, Y., et al., 2010. ADAM22, a Kv1 channel-interacting protein, recruits membrane-associated guanylate kinases to juxtaparanodes of myelinated axons. J. Neurosci. 30, 1038–1048.
Ollion, J., et al., 2013. TANGO: a generic tool for high-throughput 3D image analysis for studying nuclear organization. Bioinformatics 29, 1840–1841.
Owuor, K., et al., 2009. LGI1-associated epilepsy through altered ADAM23-dependent neuronal morphology. Mol. Cell. Neurosci. 42, 448–457.
Palacio, S., et al., 2017. Heterogeneity in Kv2 channel expression shapes action potential characteristics and firing patterns in CA1 versus CA2 hippocampal pyramidal neurons. eNeuro 4.
Perez-Riverol, Y., et al., 2022. The PRIDE database resources in 2022: a hub for mass spectrometry-based proteomics evidences. Nucleic Acids Res. 50, D543–D552.
Petit-Pedrol, M., et al., 2018. LGI1 antibodies alter Kv1.1 and AMPA receptors changing synaptic excitability, plasticity and memory. Brain : J. Neurol. 141, 3144–3159.
Pottorf 2nd, W.J., et al., 2006. Glutamate-induced protease-mediated loss of plasma membrane Ca2+ pump activity in rat hippocampal neurons. J. Neurochem. 98, 1646–1656.
Rama, S., et al., 2017. The role of axonal Kv1 channels in CA3 pyramidal cell excitability. Sci. Rep. 7, 315.
Ramirez-Franco, J., et al., 2022. Patient-derived antibodies reveal the subcellular distribution and heterogeneous interactome of LGI1. Brain : J. Neurol. 145, 3843–3858.
Rasband, M.N., et al., 2002. Clustering of neuronal potassium channels is independent of their interaction with PSD-95. J. Cell Biol. 159, 663–672.
Raus Balind, S., et al., 2019. Diverse synaptic and dendritic mechanisms of complex spike burst generation in hippocampal CA3 pyramidal cells. Nat. Commun. 10, 1859.
Reissner, K.J., et al., 2006. Synapsin I is a major endogenous substrate for protein L-isoaspartyl methyltransferase in mammalian brain. J. Biol. Chem. 281, 8389–8398.
Rimessi, A., et al., 2005. Inhibitory interaction of the 14-3-3{epsilon} protein with isoform 4 of the plasma membrane ca(2+)-ATPase pump. J. Biol. Chem. 280, 37195–37203.
Romer, S.H., et al., 2016. Activity-dependent redistribution of Kv2.1 ion channels on rat spinal motoneurons. In: Physiological Reports, 4.
Sagane, K., et al., 2008. LGI1 and LGI4 bind to ADAM22, ADAM23 and ADAM11. Int. J. Biol. Sci. 4, 387–396.

Sandhu, J., et al., 2018. Aster proteins facilitate nonvesicular plasma membrane to ER cholesterol transport in mammalian cells. Cell 175 (514–529), e20.
Satoh, A., et al., 1998. Neurabin-II/spinophilin. An actin filament-binding protein with one pdz domain localized at cadherin-based cell-cell adhesion sites. J. Biol. Chem. 273, 3470–3475.
Schulte, U., et al., 2006. The epilepsy-linked Lgi1 protein assembles into presynaptic Kv1 channels and inhibits inactivation by Kvbeta1. Neuron 49, 697–706.
Seagar, M., et al., 2017. LGI1 tunes intrinsic excitability by regulating the density of axonal Kv1 channels. Proc. Natl. Acad. Sci. USA 114, 7719–7724.
Senechal, K.R., et al., 2005. ADPEAF mutations reduce levels of secreted LGI1, a putative tumor suppressor protein linked to epilepsy. Hum. Mol. Genet. 14, 1613–1620.
Sepulveda, M.R., et al., 2006. The plasma membrane Ca2+-ATPase isoform 4 is localized in lipid rafts of cerebellum synaptic plasma membranes. J. Biol. Chem. 281, 447–453.
Sharifi, K., et al., 2011. FABP7 expression in normal and stab-injured brain cortex and its role in astrocyte proliferation. Histochem. Cell Biol. 136, 501–513.
Sharifi, K., et al., 2013. Differential expression and regulatory roles of FABP5 and FABP7 in oligodendrocyte lineage cells. Cell Tissue Res. 354, 683–695.
Sirover, M.A., 2021. The role of posttranslational modification in moonlighting glyceraldehyde-3-phosphate dehydrogenase structure and function. Amino Acids 53, 507–515.
Skraban, C.M., et al., 2017. WDR26 Haploinsufficiency causes a recognizable syndrome of intellectual disability, seizures, abnormal gait, and distinctive facial features. Am. J. Hum. Genet. 101, 139–148.
Smedfors, G., et al., 2018. A Nogo-like signaling perspective from birth to adulthood and in old age: brain expression patterns of ligands, receptors and modulators. Front. Mol. Neurosci. 11, 42.
Spiliotis, E.T., 2018. Spatial effects - site-specific regulation of actin and microtubule organization by septin GTPases. J. Cell Sci. 131.
Thomas, R.A., et al., 2018. The Nogo Receptor Ligand LGI1 Regulates Synapse Number and Synaptic Activity in Hippocampal and Cortical Neurons. eNeuro 5.
Toma-Fukai, S., Shimizu, T., 2019. Structural insights into the regulation mechanism of small GTPases by GEFs. Molecules 24.
Traub, R.D., Wong, R.K., 1982. Cellular mechanism of neuronal synchronization in epilepsy. Science 216, 745–747.
Trimmer, J.S., 2015. Subcellular localization of K+ channels in mammalian brain neurons: remarkable precision in the midst of extraordinary complexity. Neuron 85, 238–256.
Tsukada, M., et al., 2005. Doublecortin association with actin filaments is regulated by neurabin II. J. Biol. Chem. 280, 11361–11368.
Vacher, H., Trimmer, J.S., 2011. Diverse roles for auxiliary subunits in phosphorylation-dependent regulation of mammalian brain voltage-gated potassium channels. Arch. Eur. J. Physiol. 462, 631–643.
Valiyaveettil, M., et al., 2008. Novel role of the muskelin-RanBP9 complex as a nucleocytoplasmic mediator of cell morphology regulation. J. Cell Biol. 182, 727–739.
Verdura, E., et al., 2020. Complete loss of KCNA1 activity causes neonatal epileptic encephalopathy and dyskinesia. J. Med. Genet. 57, 132–137.
Vivekananda, U., et al., 2017. Kv1.1 channelopathy abolishes presynaptic spike width modulation by subthreshold somatic depolarization. Proc. Natl. Acad. Sci. USA 114, 2395–2400.
Wang, Y.H., et al., 2020. An efficient screen for cell-intrinsic factors identifies the chaperonin CCT and multiple conserved mechanisms as mediating dendrite morphogenesis. Front. Cell. Neurosci. 14, 577315.
Wang, J.L., et al., 2021. Spinophilin modulates pain through suppressing dendritic spine morphogenesis via negative control of Rac1-ERK signaling in rat spinal dorsal horn. Neurobiol. Dis. 152, 105302.
Woolfrey, K.M., Srivastava, D.P., 2016. Control of dendritic spine morphological and functional plasticity by small GTPases. Neural. Plast. 2016, 3025948.
Xu, J., Clancy, C.E., 2008. Ionic mechanisms of endogenous bursting in CA3 hippocampal pyramidal neurons: a model study. PLoS One 3, e2056.
Yamagata, A., et al., 2018. Structural basis of epilepsy-related ligand-receptor complex LGI1-ADAM22. Nat. Commun. 9, 1546.
Yamamoto, A., et al., 1998. Deficiency in protein L-isoaspartyl methyltransferase results in a fatal progressive epilepsy. J. Neurosci. 18, 2063–2074.
Ye, X.G., et al., 2021. YWHAG mutations cause childhood myoclonic epilepsy and febrile seizures: molecular sub-regional effect and mechanism. Front. Genet. 12, 632466.
Yokoi, N., et al., 2021. 14-3-3 proteins stabilize LGI1-ADAM22 levels to regulate seizure thresholds in mice. Cell Rep. 37, 110107.
Yu, Y.E., et al., 2010. Lgi1 null mutant mice exhibit myoclonic seizures and CA1 neuronal hyperexcitability. Hum. Mol. Genet. 19, 1702–1711.
Zhang, Y., et al., 2019. Neuronal function and dysfunction of CYFIP2: from actin dynamics to early infantile epileptic encephalopathy. BMB Rep. 52, 304–311.
Zhao, W.Q., Lu, B., 2007. Expression of annexin A2 in GABAergic interneurons in the normal rat brain. J. Neurochem. 100, 1211–1223.
Zhao, W.Q., et al., 2004. Specific localization of the annexin II heterotetramer in brain lipid raft fractions and its changes in spatial learning. J. Neurochem. 90, 609–620.
Zhou, L., et al., 2018. Celecoxib ameliorates seizure susceptibility in autosomal dominant lateral temporal epilepsy. J. Neurosci. 38, 3346–3357.
Zhou, L., et al., 2023. A patient-derived mutation of epilepsy-linked LGI1 increases seizure susceptibility through regulating K(v)1.1. Cell Biosci. 13, 34.
Zhu, J.X., et al., 2006. Protein repair in the brain, proteomic analysis of endogenous substrates for protein L-isoaspartyl methyltransferase in mouse brain. J. Biol. Chem. 281, 33802–33813.

**Supplementary information**

# The downregulation of $Kv_1$ channels in *Lgi1*$^{-/-}$ *mice* is accompanied by a profound modification of its Interactome and a parallel decrease in $Kv_2$ channels

Jorge Ramirez-Franco[a*], Kévin Debreux[a], Marion Sangiardi[a], Maya Belghazi[b], Yujin Kim[c], Suk-Ho Lee[c], Christian Lévêque[a], Michael Seagar[a], Oussama El Far[a*]

[a]INSERM UMR_S 1072, Unité de Neurobiologie des canaux Ioniques et de la Synapse, Aix-Marseille Université, 13015 Marseille, France

[b]Marseille Protéomique (MaP), Plateforme Protéomique IMM, CNRS FR3479, Aix-Marseille Université, 31 Chemin Joseph Aiguier 13009 Marseille, France

[c]Department of Physiology, Cell Physiology Lab, Seoul National University College of Medicine

103 Daehak-ro, Jongno-gu, Seoul, 03080, South Korea

*Corresponding author oussama.el-far@inserm.fr ; jose-jorge.ramirez-franco@univ-amu.fr

Supplementary Fig. S1; Supplementary Fig. S2; Supplementary Fig. S3; Supplementary Fig. S4; Supplementary Table S1; Supplementary Table S2; Supplementary Table S3; Supplementary sheet; Raw images of WB for Fig. 1; Raw images of WB for Fig. 2; Raw images of WB for Fig. 3; Raw images of WB for Fig. 4; Graphical abstract

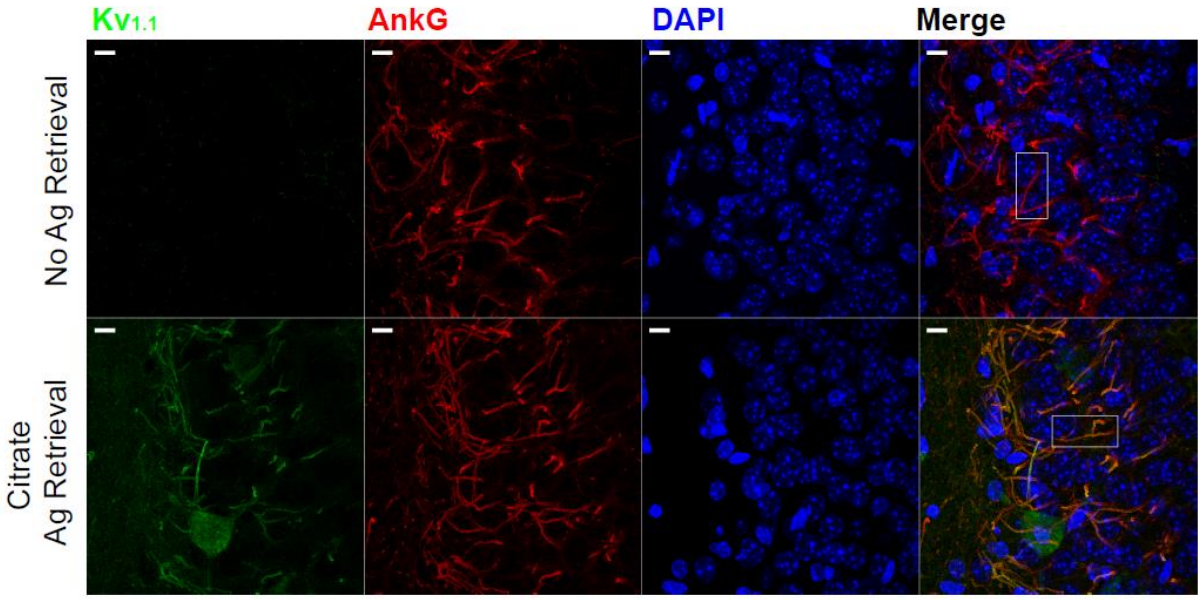


**Supplementary Fig. S1.** Antigen retrieval is necessary for specific $Kv_{1.2}$ detection in brain slices. Fixed brains of P14-P16 C57BL/6 wild-type mice were sliced and probed with anti $Kv_{1.1}$ and AnkG antibodies in the absence (upper panels) or presence (lower panels) of antigen retrieval. Note that AnKG staining was not different in both cases while $Kv_{1.1}$ staining was only possible after antigen retrieval. Inset boxes represent the regions depicted in Figure 1C. Scale bar = 12.5 µm

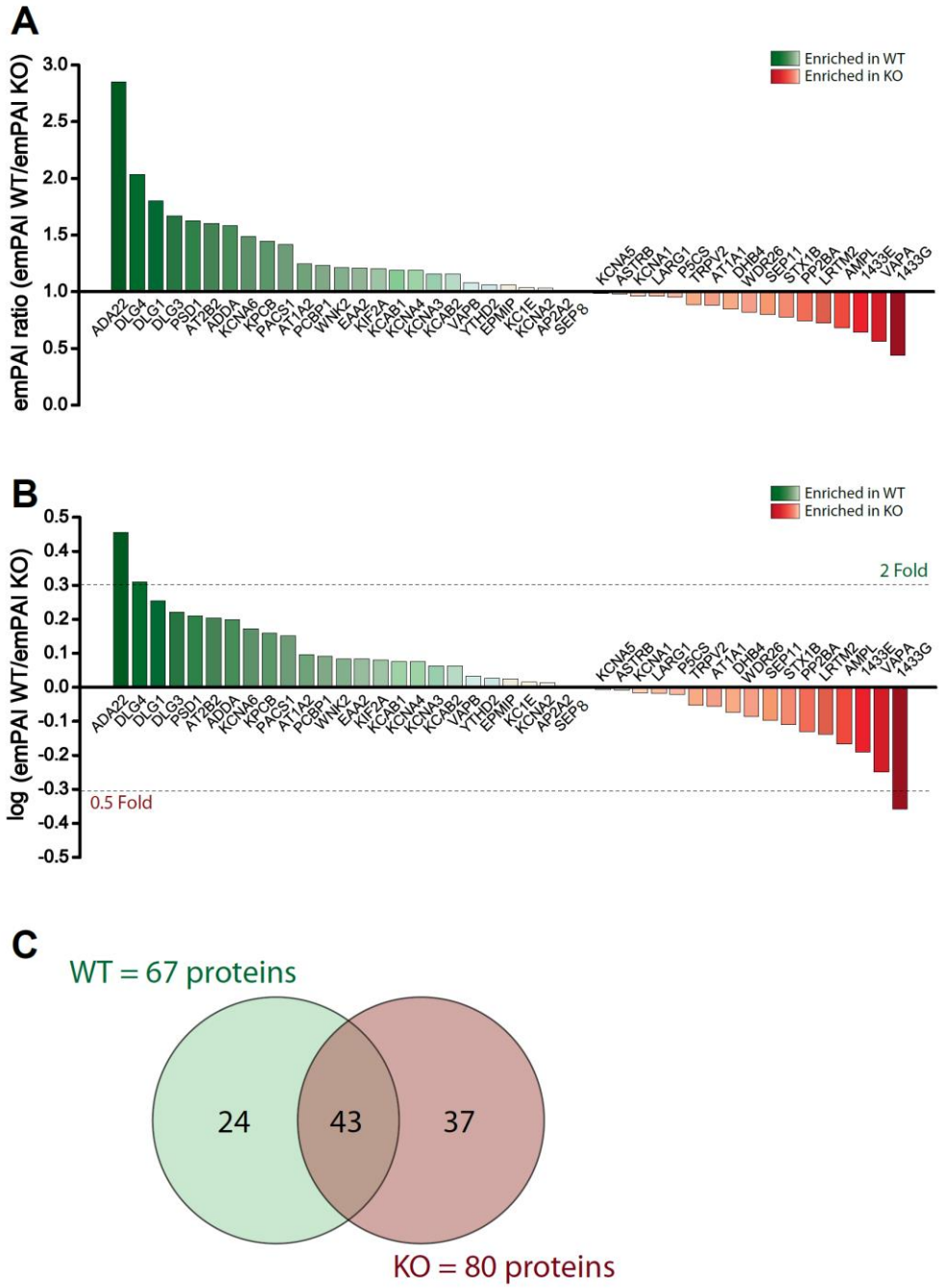


**Supplementary Fig. S2.** empAI ratios histogram of $Kv_1$ partners in WT and *Lgi1*$^{-/-}$. a) Principle up and downregulated $Kv_1$ partners in WT and *Lgi1*$^{-/-}$. b) Histograms of the log of ratios differences allowing to identify at a glance the fold change in partners enrichment. c) Venns diagram of $Kv_1$ partners in this study.

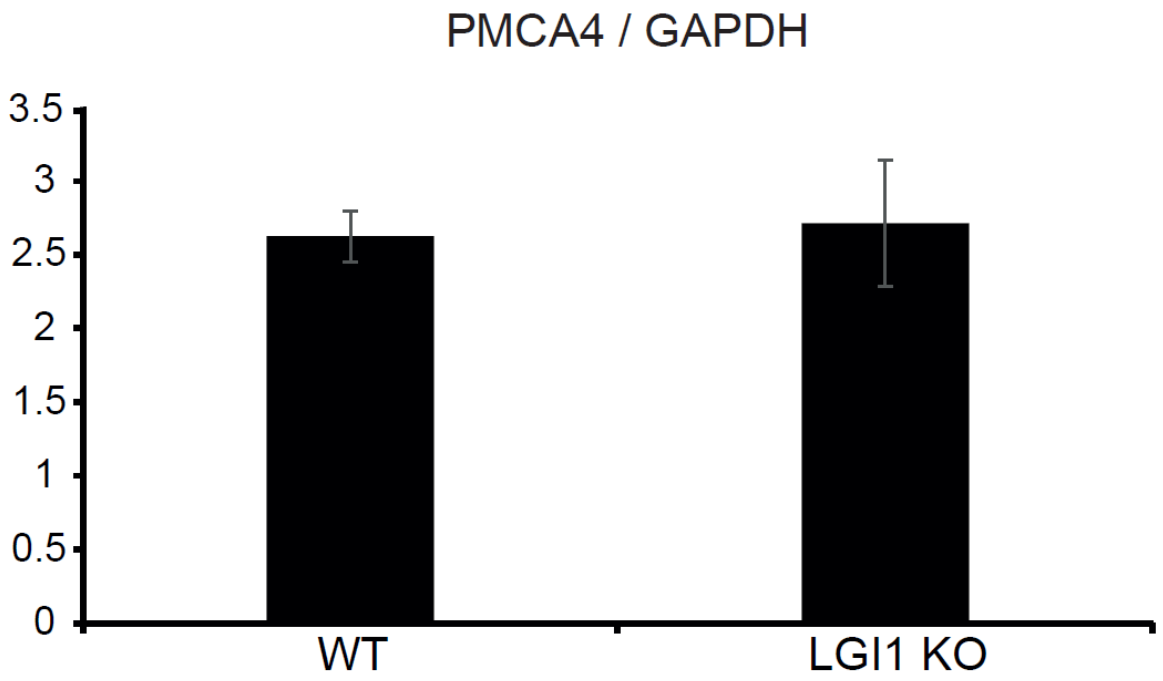


**Supplementary Fig. S3.** PMCA4/AT2B4 expression levels are not modified in *Lgi1*$^{-/-}$. The expression level of PMCA4 was probed by Western blot on brain homogenates of WT and *Lgi1*$^{-/-}$. Expression levels normalized to GAPDH signal are represented in histograms WT 2.62 ± 0.17 vs *Lgi1*$^{-/-}$ 2.71± 0.43 ($p = 0.47152$; $n = 6$; Two-tailed Mann-Whitney U test).

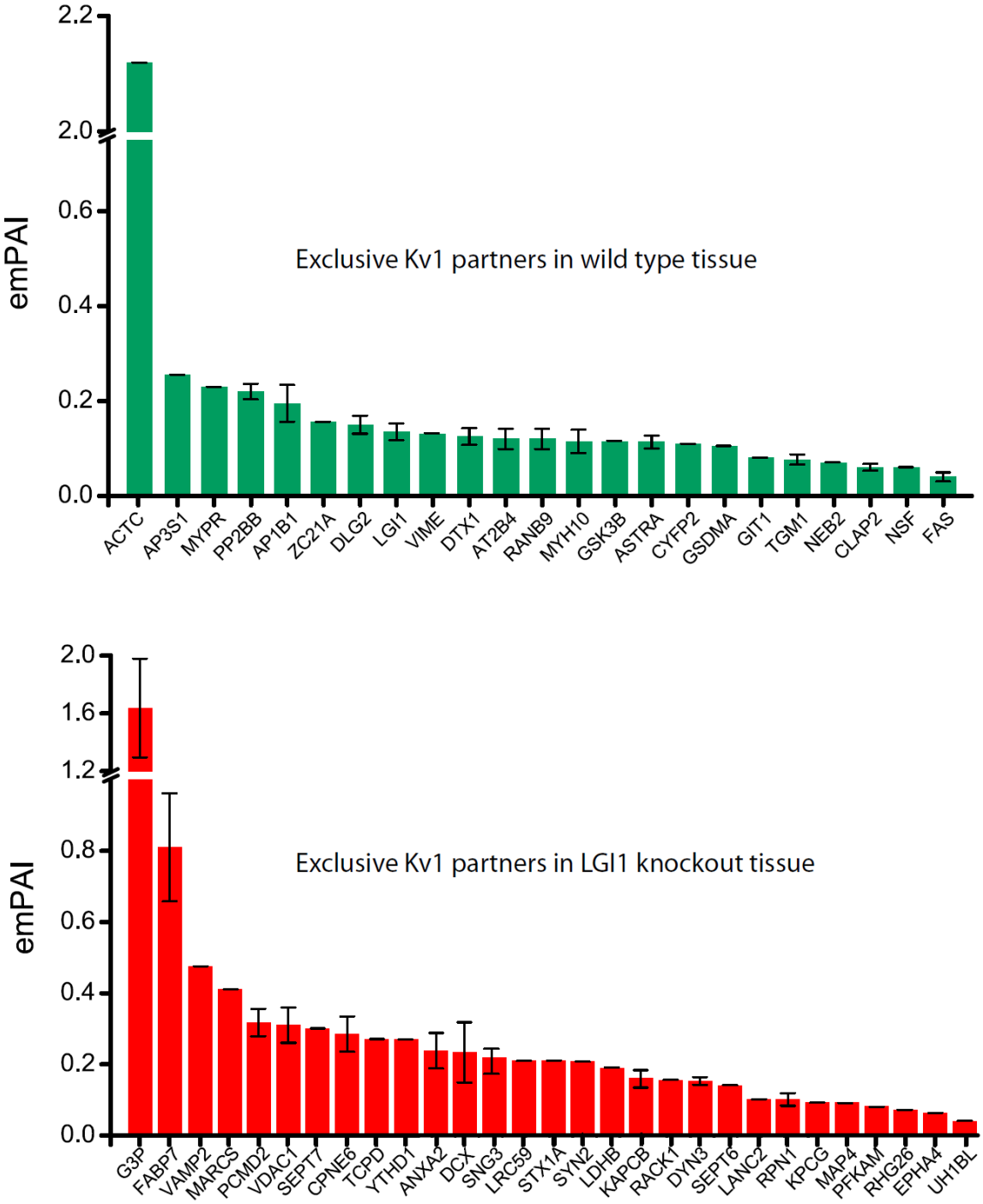


**Supplementary Fig. S4.** Exclusive $Kv_{1.2}$ partners in WT and *Lgi1*$^{-/-}$. Histograms showing exclusive immunoprecipitated protein partners of $Kv_{1.2}$ from hippocampal homogenates in WT (top, green bars) and in *Lgi1*$^{-/-}$ (bottom, red bars).

## Supplementary Table S1 Common partners in WT and Lgi1 knock out background

| Common_IDs | emPAI_WT | emPAI_KO | emPAI_WT/emPAI_KO | log(emPAI_WT/emPAI_KO) | Description |
|---|---|---|---|---|---|
| ADA22 | 0.323333333 | 0.113333333 | 2.852941176 | 0.455292817 | Disintegrin and metalloproteinase domain-containing protein 22 OS=Mus musculus GN=Adam22 |
| DLG4 | 0.733333333 | 0.36 | 2.037037037 | 0.308998925 | Disks large homolog 4 OS=Mus musculus GN=Dlg4 |
| DLG1 | 0.72 | 0.4 | 1.8 | 0.255272505 | Disks large homolog 1 OS=Mus musculus GN=Dlg1 |
| DLG3 | 0.316666667 | 0.19 | 1.666666667 | 0.22184875 | Disks large homolog 3 OS=Mus musculus GN=Dlg3 |
| PSD1 | 0.216666667 | 0.133333333 | 1.625 | 0.210853365 | PH and SEC7 domain-containing protein 1 OS=Mus musculus GN=Psd |
| AT2B2 | 0.08 | 0.05 | 1.6 | 0.204119983 | Plasma membrane calcium-transporting ATPase 2 OS=Mus musculus GN=Atp2b2 |
| ADDA | 0.126666667 | 0.08 | 1.583333333 | 0.199572355 | Alpha-adducin OS=Mus musculus GN=Add1 |
| KCNA6 | 3.293333333 | 2.213333333 | 1.487951807 | 0.172588865 | Potassium voltage-gated channel subfamily A member 6 OS=Mus musculus GN=Kcna6 |
| KPCB | 0.13 | 0.09 | 1.444444444 | 0.159700843 | Protein kinase C beta type OS=Mus musculus GN=Prkcb |
| PACS1 | 0.191666667 | 0.135 | 1.419753086 | 0.152212821 | Phosphofurin acidic cluster sorting protein 1 OS=Mus musculus GN=Pacs1 |
| AT1A2 | 0.36 | 0.288333333 | 1.248554913 | 0.096407648 | Sodium/potassium-transporting ATPase subunit alpha-2 OS=Mus musculus GN=Atp1a2 |
| WNK2 | 0.21 | 0.173333333 | 1.211538462 | 0.083337206 | Serine/threonine-protein kinase WNK2 OS=Mus musculus GN=Wnk2 |
| EAA2 | 0.23 | 0.19 | 1.210526316 | 0.082974235 | Excitatory amino acid transporter 2 OS=Mus musculus GN=Slc1a2 |
| KIF2A | 0.846666667 | 0.703333333 | 1.203791469 | 0.080551261 | Kinesin-like protein KIF2A OS=Mus musculus GN=Kif2a |
| KCAB1 | 3.426666667 | 2.876666667 | 1.191193511 | 0.075982319 | Voltage-gated potassium channel subunit beta-1 OS=Mus musculus GN=Kcnab1 |
| KCNA4 | 1.56 | 1.31 | 1.190839695 | 0.075853303 | Potassium voltage-gated channel subfamily A member 4 OS=Mus musculus GN=Kcna4 |
| KCNA3 | 3.153333333 | 2.723333333 | 1.157894737 | 0.06366908 | Potassium voltage-gated channel subfamily A member 3 OS=Mus musculus GN=Kcna3 |
| KCAB2 | 14.25333333 | 12.31333333 | 1.157552788 | 0.063540805 | Voltage-gated potassium channel subunit beta-2 OS=Mus musculus GN=Kcnab2 |
| VAPB | 0.366666667 | 0.34 | 1.078431373 | 0.032792513 | Vesicle-associated membrane protein-associated protein B OS=Mus musculus GN=Vapb |
| YTHD2 | 0.313333333 | 0.295 | 1.062146893 | 0.026184583 | YTH domain-containing family protein 2 OS=Mus musculus GN=Ythdf2 |
| EPMIP | 3.326666667 | 3.14 | 1.059447983 | 0.025079638 | EPM2A-interacting protein 1 OS=Mus musculus GN=Epm2aip1 |
| KC1E | 0.145 | 0.14 | 1.035714286 | 0.015239967 | Casein kinase I isoform epsilon OS=Mus musculus GN=Csnk1e |
| KCNA2 | 2.896666667 | 2.81 | 1.03084223 | 0.013192202 | Potassium voltage-gated channel subfamily A member 2 OS=Mus musculus GN=Kcna2 |
| AP2A2 | 0.255 | 0.253333333 | 1.006578947 | 0.002847843 | AP-2 complex subunit alpha-2 OS=Mus musculus GN=Ap2a2 |
| SEPT8 | 0.14 | 0.14 | 1 | 0 | Septin-8 OS=Mus musculus GN=Sept8 |
| KCNA5 | 0.446666667 | 0.453333333 | 0.985294118 | -0.00643411 | Potassium voltage-gated channel subfamily A member 5 OS=Mus musculus GN=Kcna5 |
| ASTRB | 0.643333333 | 0.656666667 | 0.979695431 | -0.008908917 | Protein Aster-B OS=Mus musculus GN=Gramd1b |
| KCNA1 | 2.83 | 2.94 | 0.962585034 | -0.016560895 | Potassium voltage-gated channel subfamily A member 1 OS=Mus musculus GN=Kcna1 |
| LARG1 | 0.496666667 | 0.516666667 | 0.961290323 | -0.01714543 | LARGE xylosyl- and glucuronyltransferase 1 OS=Mus musculus GN=Large1 |
| P5CS | 0.42 | 0.44 | 0.954545455 | -0.020203386 | Delta-1-pyrroline-5-carboxylate synthase OS=Mus musculus GN=Aldh18a1 |
| TRPV2 | 0.39 | 0.44 | 0.886363636 | -0.052388069 | Transient receptor potential cation channel subfamily V member 2 OS=Mus musculus GN=Trpv2 |
| AT1A1 | 0.27 | 0.306666667 | 0.880434783 | -0.055302808 | Sodium/potassium-transporting ATPase subunit alpha-1 OS=Mus musculus GN=Atp1a1 |
| DHB4 | 0.685 | 0.81 | 0.845679012 | -0.072794447 | Peroxisomal multifunctional enzyme type 2 OS=Mus musculus GN=Hsd17b4 |
| WDR26 | 0.166666667 | 0.203333333 | 0.819672131 | -0.086359831 | WD repeat-containing protein 26 OS=Mus musculus GN=Wdr26 |
| SEP11 | 0.14 | 0.175 | 0.8 | -0.096910013 | Septin-11 OS=Mus musculus GN=Sept11 |
| STX1B | 0.21 | 0.27 | 0.777777778 | -0.109144469 | Syntaxin-1B OS=Mus musculus GN=Stx1b |
| PP2BA | 0.245 | 0.33 | 0.742424242 | -0.129347856 | Serine/threonine-protein phosphatase 2B catalytic subunit alpha isoform OS=Mus musculus GN=Ppp3ca |
| LRTM2 | 0.593333333 | 0.816666667 | 0.726530612 | -0.138746082 | Leucine-rich repeat and transmembrane domain-containing protein 2 OS=Mus musculus GN=Lrtm2 |
| AMPL | 0.62 | 0.91 | 0.681318681 | -0.166649703 | Cytosol aminopeptidase OS=Mus musculus GN=Lap3 |
| 1433E | 0.386666667 | 0.6 | 0.644444444 | -0.190814516 | 14-3-3 protein epsilon OS=Mus musculus GN=Ywhae |
| VAPA | 1.21 | 2.146666667 | 0.563664596 | -0.248979242 | Vesicle-associated membrane protein-associated protein A OS=Mus musculus GN=Vapa |
| 1433G | 0.325 | 0.74 | 0.439189189 | -0.357348359 | 14-3-3 protein gamma OS=Mus musculus GN=Ywhag |

**Supplementary Table S2. Specific $Kv_{1.2}$ partners in WT background**

| ID | emPAI | SEM | Description |
|---|---|---|---|
| ACTC | 2.12 | 0.00 | Actin, alpha cardiac muscle 1 OS=Mus musculus GN=Actc1 |
| AP3S1 | 0.255 | 0.00 | AP-3 complex subunit sigma-1 OS=Mus musculus GN=Ap3s1 |
| MYPR | 0.23 | 0.00 | Myelin proteolipid protein OS=Mus musculus GN=Plp1 |
| PP2BB | 0.22 | 0.02 | Serine/threonine-protein phosphatase 2B catalytic subunit beta isoform OS=Mus musculus GN=Ppp3cb |
| AP1B1 | 0.195 | 0.04 | AP-1 complex subunit beta-1 OS=Mus musculus GN=Ap1b1 |
| ZC21A | 0.155 | 0.00 | Zinc finger C2HC domain-containing protein 1A OS=Mus musculus GN=Zc2hc1a |
| DLG2 | 0.15 | 0.02 | Disks large homolog 2 OS=Mus musculus GN=Dlg2 |
| LGI1 | 0.135 | 0.02 | Leucine-rich glioma-inactivated protein 1 OS=Mus musculus GN=Lgi1 |
| VIME | 0.13 | 0.00 | Vimentin OS=Mus musculus GN=Vim |
| DTX1 | 0.125 | 0.02 | E3 ubiquitin-protein ligase DTX1 OS=Mus musculus GN=Dtx1 |
| AT2B4 | 0.12 | 0.02 | Plasma membrane calcium-transporting ATPase 4 OS=Mus musculus GN=Atp2b4 |
| RANB9 | 0.12 | 0.02 | Ran-binding protein 9 OS=Mus musculus GN=Ranbp9 |
| MYH10 | 0.115 | 0.02 | Myosin-10 OS=Mus musculus GN=Myh10 |
| GSK3B | 0.115 | 0.00 | Glycogen synthase kinase-3 beta OS=Mus musculus GN=Gsk3b |
| ASTRA | 0.113333333 | 0.01 | Protein Aster-A OS=Mus musculus GN=Gramd1a |
| CYFP2 | 0.11 | 0.00 | Cytoplasmic FMR1-interacting protein 2 OS=Mus musculus GN=Cyfip2 |
| GSDMA | 0.105 | 0.00 | Gasdermin-A OS=Mus musculus GN=Gsdma PE=2 SV=1 |
| GIT1 | 0.08 | 0.00 | ARF GTPase-activating protein GIT1 OS=Mus musculus GN=Git1 |
| TGM1 | 0.076666667 | 0.01 | Protein-glutamine gamma-glutamyltransferase K OS=Mus musculus GN=Tgm1 |
| NEB2 | 0.07 | 0.00 | Neurabin-2 OS=Mus musculus GN=Ppp1r9b |
| CLAP2 | 0.06 | 0.01 | CLIP-associating protein 2 OS=Mus musculus GN=Clasp2 |
| NSF | 0.06 | 0.00 | Vesicle-fusing ATPase OS=Mus musculus GN=Nsf |
| FAS | 0.04 | 0.01 | Fatty acid synthase OS=Mus musculus GN=Fasn |

**Supplementary Table S3. Specific $Kv_{1.2}$ partners in Lgi1 know out background**

| ID | emPAI | SEM | Description |
|---|---|---|---|
| G3P | 1.638333333 | 0.34 | Glyceraldehyde-3-phosphate dehydrogenase OS=Mus musculus GN=Gapdh |
| FABP7 | 0.81 | 0.15 | Fatty acid-binding protein, brain OS=Mus musculus GN=Fabp7 |
| VAMP2 | 0.475 | 0.00 | Vesicle-associated membrane protein 2 OS=Mus musculus GN=Vamp2 |
| MARCS | 0.41 | 0.00 | Myristoylated alanine-rich C-kinase substrate OS=Mus musculus GN=Marcks |
| PCMD2 | 0.3175 | 0.04 | Protein-L-isoaspartate O-methyltransferase domain-containing protein 2 OS=Mus musculus GN=Pcmtd2 |
| VDAC1 | 0.31 | 0.05 | Voltage-dependent anion-selective channel protein 1 OS=Mus musculus GN=Vdac1 |
| SEPT7 | 0.3 | 0.00 | Septin-7 OS=Mus musculus GN=Sept7 |
| CPNE6 | 0.285 | 0.05 | Copine-6 OS=Mus musculus GN=Cpne6 |
| TCPD | 0.27 | 0.00 | T-complex protein 1 subunit delta OS=Mus musculus GN=Cct4 |
| YTHD1 | 0.27 | 0.00 | YTH domain-containing family protein 1 OS=Mus musculus GN=Ythdf1 |
| ANXA2 | 0.238333333 | 0.05 | Annexin A2 OS=Mus musculus GN=Anxa2 |
| DCX | 0.233333333 | 0.08 | Neuronal migration protein doublecortin OS=Mus musculus GN=Dcx |
| SNG3 | 0.22 | 0.00 | Synaptogyrin-3 OS=Mus musculus GN=Syngr3 |
| LRC59 | 0.21 | 0.00 | Leucine-rich repeat-containing protein 59 OS=Mus musculus GN=Lrrc59 |
| STX1A | 0.21 | 0.00 | Syntaxin-1A OS=Mus musculus GN=Stx1a |
| SYN2 | 0.208333333 | 0.04 | Synapsin-2 OS=Mus musculus GN=Syn2 |
| LDHB | 0.19 | 0.00 | L-lactate dehydrogenase B chain OS=Mus musculus GN=Ldhb |
| KAPCB | 0.16 | 0.02 | cAMP-dependent protein kinase catalytic subunit beta OS=Mus musculus GN=Prkacb |
| RACK1 | 0.155 | 0.00 | Receptor of activated protein C kinase 1 OS=Mus musculus GN=Rack1 |
| DYN3 | 0.153333333 | 0.01 | Dynamin-3 OS=Mus musculus GN=Dnm3 |
| SEPT6 | 0.14 | 0.00 | Septin-6 OS=Mus musculus GN=Sept6 |
| LANC2 | 0.1 | 0.00 | LanC-like protein 2 OS=Mus musculus GN=Lancl2 |
| RPN1 | 0.1 | 0.02 | Dolichyl-diphosphooligosaccharide--protein glycosyltransferase subunit 1 OS=Mus musculus GN=Rpn1 |
| KPCG | 0.09 | 0.00 | Protein kinase C gamma type OS=Mus musculus GN=Prkcg |
| MAP4 | 0.09 | 0.00 | Microtubule-associated protein 4 OS=Mus musculus GN=Map4 |
| PFKAM | 0.08 | 0.00 | ATP-dependent 6-phosphofructokinase, muscle type OS=Mus musculus GN=Pfkm |
| RHG26 | 0.07 | 0.00 | Rho GTPase-activating protein 26 OS=Mus musculus GN=Arhgap26 |
| EPHA4 | 0.06 | 0.00 | Ephrin type-A receptor 4 OS=Mus musculus GN=Epha4 |
| UH1BL | 0.04 | 0.00 | UHRF1-binding protein 1-like OS=Mus musculus GN=Uhrf1bp1l |

Supplementary sheet 1/3

| $Kv_1$ partners (immunoprecipitation with anti $Kv_{1.2}$ from mouse brain homogenates of WT versus LGI1 knock out | | | | | | | | | |
|---|---|---|---|---|---|---|---|---|---|
| **Only in WT** | **emPAI** | **Only in KO_LGI1** | **emPAI** | **Common WT/LGI1_KO; Increased in KO** | **Ratio_emPAI WT/KO** | **Common; Decreased in KO** | **Ratio_emPAI WT/KO** | **Common WT/LGI1_KO; Stable** | **Rattio_emPAI WT/KO** |
| ACTC_MOUSE | 2.12 | Flgi | 1.638333333 | KCNA5_MOUSE | 0.985294118 | ADA22_MOUSE | 2.852941176 | SEPT8 | 1 |
| AP3S1_MOUSE | 0.255 | FABP7_MOUSE | 0.81 | ASTRB_MOUSE | 0.979695431 | DLG4_MOUSE | 2.037037037 | KCAB1_MOUSE | 1.191193511 |
| MYPR_MOUSE | 0.23 | ATPB_MOUSE | 0.755 | KCNA1_MOUSE | 0.962585034 | DLG1_MOUSE | 1.8 | KCNA4_MOUSE | 1.190839695 |
| PP2BB_MOUSE | 0.22 | VAMP2_MOUSE | 0.475 | LARG1_MOUSE | 0.961290323 | DLG3_MOUSE | 1.666666667 | KCNA3_MOUSE | 1.157894737 |
| AP1B1_MOUSE | 0.195 | MARCS_MOUSE | 0.41 | P5CS_MOUSE | 0.954545455 | PSD1_MOUSE | 1.625 | KCAB2_MOUSE | 1.157552788 |
| DLG2_MOUSE | 0.15 | PCMD2_MOUSE | 0.3175 | TRPV2_MOUSE | 0.886363636 | AT2B2_MOUSE | 1.6 | VAPB_MOUSE | 1.078431373 |
| LGI1_MOUSE | 0.135 | VDAC1_MOUSE | 0.31 | AT1A1_MOUSE | 0.880434783 | ADDA_MOUSE | 1.583333333 | EPMIP_MOUSE | 1.059447983 |
| VIME_MOUSE | 0.13 | SEP_7_MOUSE | 0.3 | DHB4_MOUSE | 0.845679012 | KCNA6_MOUSE | 1.487951807 | KC1E_MOUSE | 1.035714286 |
| DTX1_MOUSE | 0.125 | CPNE6_MOUSE | 0.29 | WDR26_MOUSE | 0.819672131 | KPCB_MOUSE | 1.444444444 | KCNA2_MOUSE | 1.03084223 |
| AT2B4_MOUSE | 0.12 | TCPD_MOUSE | 0.27 | SEP11_MOUSE | 0.8 | PACS1_MOUSE | 1.419753086 | AP2A2_MOUSE | 1.006578947 |
| RANB9_MOUSE | 0.12 | ANXA2_MOUSE | 0.24 | STX1B_MOUSE | 0.777777778 | AT1A2_MOUSE | 1.248554913 | | |
| MYH10_MOUSE | 0.115 | DCX_MOUSE | 0.23 | PP2BA_MOUSE | 0.742424242 | WNK2_MOUSE | 1.211538462 | | |
| GSK3B_MOUSE | 0.115 | SNG3_MOUSE | 0.22 | LRTM2_MOUSE | 0.726530612 | **EAA2_MOUSE** | **1.210526316** | | |
| ASTRA_MOUSE | 0.1133 | LRC59_MOUSE | 0.21 | AMPL_MOUSE | 0.681318681 | KIF2A_MOUSE | 1.203791469 | | |
| CYFP2_MOUSE | 0.11 | STX1A_MOUSE | 0.21 | 1433E_MOUSE | 0.644444444 | | | | |
| GSDMA_MOUSE | 0.105 | SYN2_MOUSE | 0.21 | **VAPA_MOUSE** | **0.563664596** | | | | |
| TGM1_MOUSE | 0.0766 | LDHB_MOUSE | 0.19 | 1433G_MOUSE | 0.439189189 | | | | |
| NEB2_MOUSE | 0.07 | KAPCB_MOUSE | 0.16 | | | | | | |
| CLAP2_MOUSE | 0.06 | RACK1_MOUSE | 0.16 | | | | | | |
| NSF_MOUSE | 0.06 | DYN3_MOUSE | 0.15 | | | | | | |
| FAS_MOUSE | 0.04 | SEP_6_MOUSE | 0.14 | | | | | | |
| GIT1_MOUSE | 0.008 | LANC2_MOUSE | 0.10 | | | | | | |
| | | RPN1_MOUSE | 0.10 | | | | | | |
| | | KPCG_MOUSE | 0.09 | | | | | | |
| | | MAP4_MOUSE | 0.09 | | | | | | |
| | | PFKAM_MOUSE | 0.08 | | | | | | |
| | | RHG26_MOUSE | 0.07 | | | | | | |
| | | GRP75_MOUSE | 0.07 | | | | | | |
| | | EPHA4_MOUSE | 0.06 | | | | | | |
| | | UH1BL_MOUSE | 0.04 | | | | | | |

# Supplementary sheet 2/3

**Functional properties of candidate proteins classified using the pantherdb web site (www.pantherdb.org)**

| | | emPAI | Ion / Amino acid transport | Enzyme | Molecular motor | Cell membrane | Golgi | Lipid binding / transport / metabolism | Extracellular | Cytoskeletal / cytoskeletal organisation | Adaptor protein | Cytoplasmic | Pore forming activity | Chaperone | Axon guidance | Catabolic process | Axonal and dendritic morphogenesis | Endocytosis | Exocytosis | Receptor clustering | Raft assembly | PDZ interaction | Phospholipid binding |
|---|---|---|---|---|---|---|---|---|---|---|---|---|---|---|---|---|---|---|---|---|---|---|---|
| Associated with Kv1 only in WT mice | ACTC_MOUSE | 2.12 | | | | | | | | Y | Y | | | | | | | | | | | | |
| | AP3S1_MOUSE | 0.255 | | | | | Y | | | | Y | | | | | | | | | | | | |
| | MYPR_MOUSE | 0.23 | | | | Y | | | | | | | | | | | Y | | Y | | | | |
| | PP2BB_MOUSE | 0.22 | | Y | | | | | | | | Y | | | | | | Y | Y | | | | |
| | AP1B1_MOUSE | 0.195 | | | | | | | | | Y | | | | | | | | | | | | |
| | DLG2_MOUSE | 0.15 | | | | Y | | | | | | | | | | | | | | Y | | | |
| | LGI1_MOUSE | 0.135 | | | | | | | Y | | | | | | | | Y | | | | | | |
| | VIME_MOUSE | 0.13 | | | | Y | | | | Y | | | | | | | Y | | | | | | |
| | DTX1_MOUSE | 0.125 | | Y | | | | | | | | Y | | Y | | | | | | | | | |
| | AT2B4_MOUSE | 0.12 | Y | | | Y | | | | | | | | | | Y | | | | | | | |
| | RANB9_MOUSE | 0.12 | | | | | | | | Y | | | | | | Y | | | | | | | |
| | MYH10_MOUSE | 0.115 | | | | | | | | Y | | | | | | | | | | | | | |
| | GSK3B_MOUSE | 0.115 | | Y | | | | | | Y | | | | | | Y | Y | | Y | | | | |
| | ASTRA_MOUSE | 0.1133 | | | | | | Y | | | | | | | | | | | | | | | |
| | CYFP2_MOUSE | 0.11 | | | | | | | | Y | | Y | | | | | Y | | | | | | |
| | GSDMA_MOUSE | 0.105 | | | | | | Y | | | | | Y | | | | | | | | | | |
| | TGM1_MOUSE | 0.0766 | | Y | | | | | | | | | | | | | | | | | | | |
| | NEB2_MOUSE | 0.07 | | Y | | Y | | | | Y | | | | | | | Y | | | | | | |
| | CLAP2_MOUSE | 0.06 | | | | Y | Y | | | Y | | | | | | | Y | | Y | | | | |
| | NSF_MOUSE | 0.06 | | Y | | | Y | | | | | | | | | Y | | Y | | | | | |
| | FAS_MOUSE | 0.04 | | Y | | | | Y | | | | Y | | | | | | | | | | | |
| | GIT1_MOUSE | 0.008 | | Y | | | | | | Y | | | | | | Y | Y | | Y | | | | |
| | | | | | | | | | | | | | | | | | | | | | | | |
| | | emPAI | | | | | | | | | | | | | | | | | | | | | |
| Associated with Kv1 only in Lgi1$^{-/-}$ | G3P_MOUSE | 1.638333333 | | Y | | | | | | Y | | | | | | | | | | | | | |
| | FABP7_MOUSE | 0.81 | | | | | | Y | | | | | | | | | | | | | | | |
| | ATPB_MOUSE | 0.755 | Y | | | | | | | | | | | | | | | Y | | | | | |
| | VAMP2_MOUSE | 0.475 | | | | | | | | | | | | | | | | Y | Y | | | | Y |
| | MARCS_MOUSE | 0.41 | | | | | | | | Y | | | | | | | Y | | | | | | Y |
| | PCMD2_MOUSE | 0.3175 | | | | | | | | | | | | | | | | | | | | | |
| | VDAC1_MOUSE | 0.31 | Y | | | | | | | | | | | | | | | | | | | | |
| | SEP_7_MOUSE | 0.3 | | | | | | | | Y | | | | | | | | | | | | | |
| | CPNE6_MOUSE | 0.29 | | | | Y | | Y | | | | | | | | | Y | | | | | | Y |
| | TCPD_MOUSE | 0.27 | | | | | | | | Y | | | | Y | | | | | | | | | |
| | ANXA2_MOUSE | 0.24 | | | | | | | Y | | | | | | | Y | | Y | Y | | Y | | Y |
| | DCX_MOUSE | 0.23 | | | | | | | | | | | | | | | Y | Y | | | | | |
| | SNG3_MOUSE | 0.22 | | | | | | | | | | | | | | | | | Y | | | | |
| | LRC59_MOUSE | 0.21 | | | | | | | | | | | | | | | | | | | | | |
| | STX1A_MOUSE | 0.21 | | | | | | | | | | | | | | | | Y | Y | | | | |
| | SYN2_MOUSE | 0.21 | | | | | | | | | | | | | | | | | Y | | | | |
| | LDHB_MOUSE | 0.19 | | Y | | | | | | | | | | | | | | | | | | | |
| | KAPCB_MOUSE | 0.16 | | Y | | | | | | | | | | | Y | | | | | | | | |
| | RACK1_MOUSE | 0.16 | | | | | | | | | | | | | | Y | | | | | | | |
| | DYN3_MOUSE | 0.15 | | | Y | | | | | | | | | | | | Y | Y | | | | | |
| | SEP_6_MOUSE | 0.14 | | | | | | | | | | | | | | | | | | | | | |
| | LANC2_MOUSE | 0.10 | | | | Y | | | | | | | | | | | | | | | | | |
| | RPN1_MOUSE | 0.10 | | Y | | | | | | | | | | | | | | | | | | | |
| | KPCG_MOUSE | 0.09 | | Y | | | | | | | | | | | | Y | | | Y | | | | |
| | MAP4_MOUSE | 0.09 | | | | | | | | Y | | | | | | | | | | | | | |
| | PFKAM_MOUSE | 0.08 | | Y | | | | | | | | | | | | Y | | | | | | | |
| | RHG26_MOUSE | 0.07 | | | | | | | | Y | | Y | | | | | | | | | | | Y |
| | GRP75_MOUSE | 0.07 | | | | | | | | | | | | Y | | | | | | | | | |
| | EPHA4_MOUSE | 0.06 | | | | Y | | | | | | | | | Y | Y | Y | | | | | | |
| | UH1BL_MOUSE | 0.04 | | | | | | | | | | Y | | | | | | | | | | | |

# Supplementary sheet 3/3

**Functional properties of candidate proteins classified using the pantherdb web site (www.pantherdb.org)**

| | | emPAI WT/KO | Ion / Amino acid transport | Enzyme | Molecular motor | Cell membrane | Golgi | Lipid binding / transport / metabolism | Extracellular | Cytoskeletal / cytoskeletal organisation | Adaptor protein | Cytoplasmic | Pore forming activity | Chaperone | Axon guidance | Catabolic process | Axonal and dendritic morphogenesis | Endocytosis | Exocytosis | Receptor clustering | Raft assembly | PDZ interaction | Phospholipid binding |
|---|---|---|---|---|---|---|---|---|---|---|---|---|---|---|---|---|---|---|---|---|---|---|---|
| Common partners decreased in *Lgi*$^{-/-}$ | ADA22_MOUSE | 2.852941176 | | | | Y | | | | | | | | | | | | | | | | Y | |
| | DLG4_MOUSE | 2.037037037 | | | | Y | | | | | | | | | | | | | | | | | |
| | DLG1_MOUSE | 1.8 | | | | Y | | | | | | | | | | | | | | | | | |
| | DLG3_MOUSE | 1.666666667 | | | | Y | | | | | | | | | | | | | | | | | |
| | PSD1_MOUSE | 1.625 | | | | Y | | | | | | | | | | | | | | | | | Y |
| | AT2B2_MOUSE | 1.6 | Y | | | Y | | | | | | | | | | | | | | | | Y | |
| | ADDA_MOUSE | 1.583333333 | | | | Y | | | | Y | | | | | | | | | | | | | |
| | KCNA6_MOUSE | 1.487951807 | Y | | | Y | | | | | | | | | | | | | | | | Y | |
| | KPCB_MOUSE | 1.444444444 | | Y | | | | | | | | | | | | | | | | | | | |
| | PACS1_MOUSE | 1.419753086 | | | | | Y | | | | | | | | | | | | | | | | |
| | AT1A2_MOUSE | 1.248554913 | Y | | | Y | | | | | | | | | | | | | | | | | |
| | WNK2_MOUSE | 1.211538462 | | Y | | Y | | | | | | | | | | | | | | | | | |
| | EAA2_MOUSE | 1.210526316 | Y (Slc1a2) | | | Y | | | | | | | | | | | | | | | | | |
| | KIF2A_MOUSE | 1.203791469 | | | Y | | | | | Y | | | | | | | | | | | | | |

| | | emPAI | | | | | | | | | | | | | | | | | | | | | |
|---|---|---|---|---|---|---|---|---|---|---|---|---|---|---|---|---|---|---|---|---|---|---|---|
| Common partners increased in *Lgi*$^{-/-}$ | KCNA5_MOUSE | 0.985294118 | Y | | | Y | | | | | | | | | | | | | | | | Y | |
| | ASTRB_MOUSE | 0.979695431 | | | | Y | | Y | | | | | | | | | | | | | | | Y |
| | KCNA1_MOUSE | 0.962585034 | Y | | | Y | | | | | | | | | | | | | | | | Y | |
| | LARG1_MOUSE | 0.961290323 | | Y | | | Y | | | | | | | | | | | | | | | | |
| | P5CS_MOUSE | 0.954545455 | | Y | | | | | | | | | | | | | | | | | | | |
| | TRPV2_MOUSE | 0.886363636 | Y | | | Y | | | | | | | | | | | Y | | | | | | |
| | AT1A1_MOUSE | 0.880434783 | Y | | | Y | | | | | | | | | | | | | | | | | |
| | DHB4_MOUSE | 0.845679012 | | Y | | | | Y | | | | | | | | | | | | | | | |
| | WDR26_MOUSE | 0.819672131 | | | | | | | | | | Y | | | | Y | | | | | | | |
| | SEP11_MOUSE | 0.8 | | | | | | | | Y | | | | | | | | | | | | | |
| | STX1B_MOUSE | 0.777777778 | | | | Y | | | | | | | | | | | | | Y | | | | |
| | PP2BA_MOUSE | 0.742424242 | | Y | | | | | | | | | | | | | | Y | | | | | |
| | LRTM2_MOUSE | 0.726530612 | | | | Y | | | | | | | | | Y | | | | | | | | |
| | AMPL_MOUSE | 0.681318681 | | Y | | | | | | | | | | | | Y | | | | | | | |
| | 1433E_MOUSE | 0.644444444 | | Y | | | | | | | | Y | | | | | | | | | | | |
| | VAPA_MOUSE | 0.563664596 | | | | | Y | | | | | | | | | | | | | | | | Y |
| | 1433G_MOUSE | 0.439189189 | | Y | | | | | | | | Y | | | | | | | | | | | |

Raw images of western blots in Figure 1

Whole brain

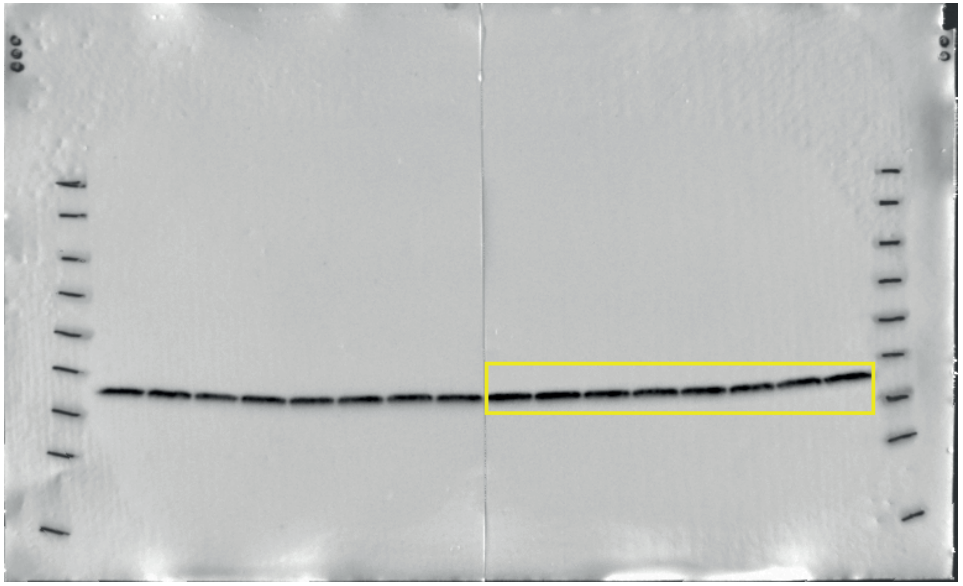

Composite_GAPDH_red

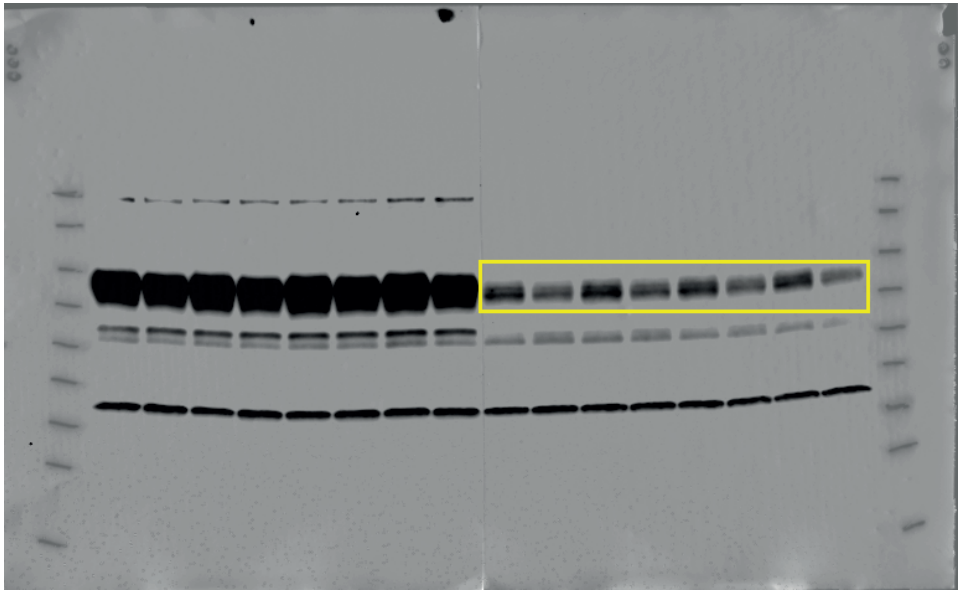

Composite_Kv1-1_green

Hippocampus

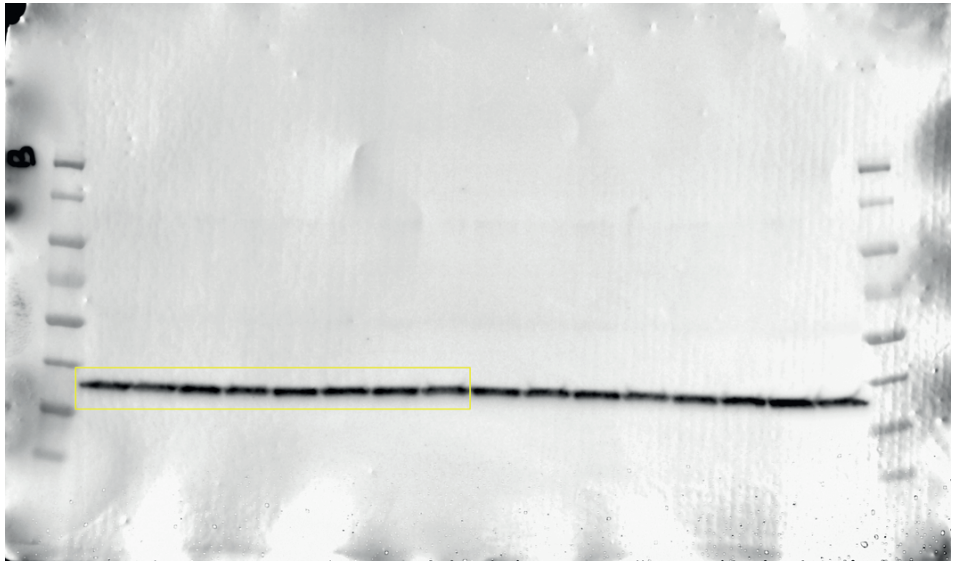

Composite_GAPDH_red

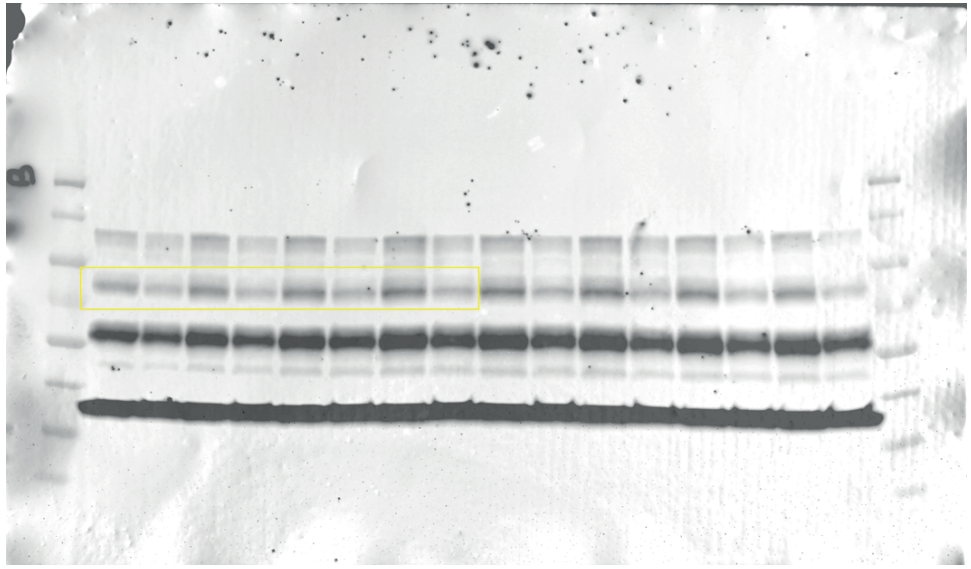

Composite_Kv1-1_green

Raw images of western blots in Figure 2

Whole brain

Composite_red_GAPDH

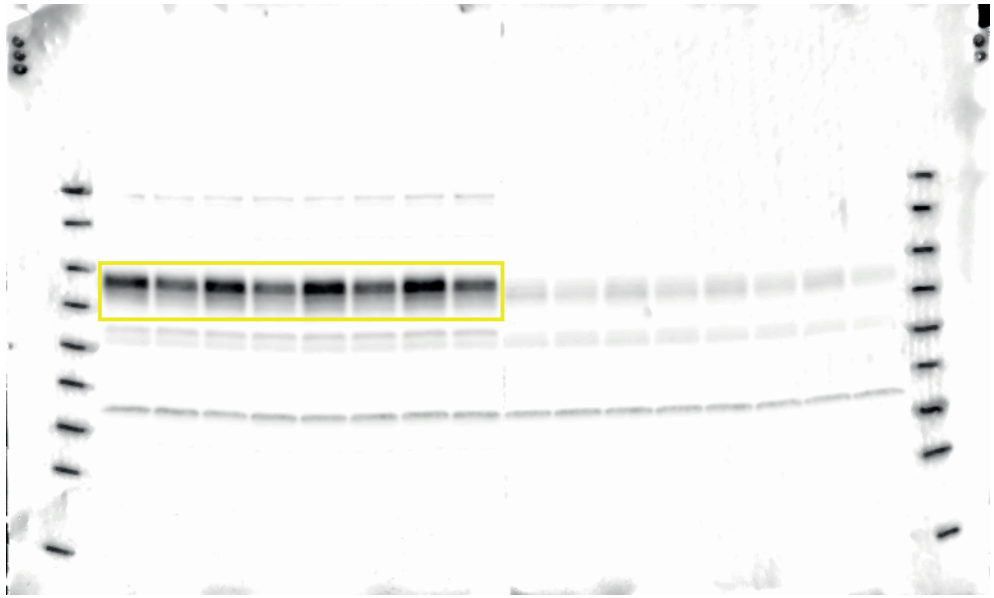

Composite_Green_Kv1.2

Hippocampus

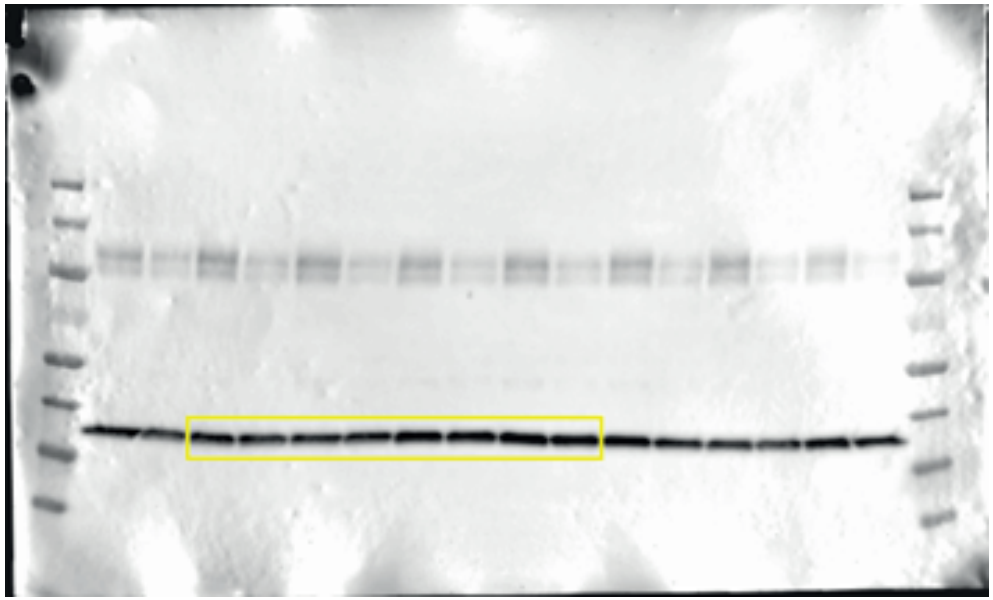

Composite_red_GAPDH

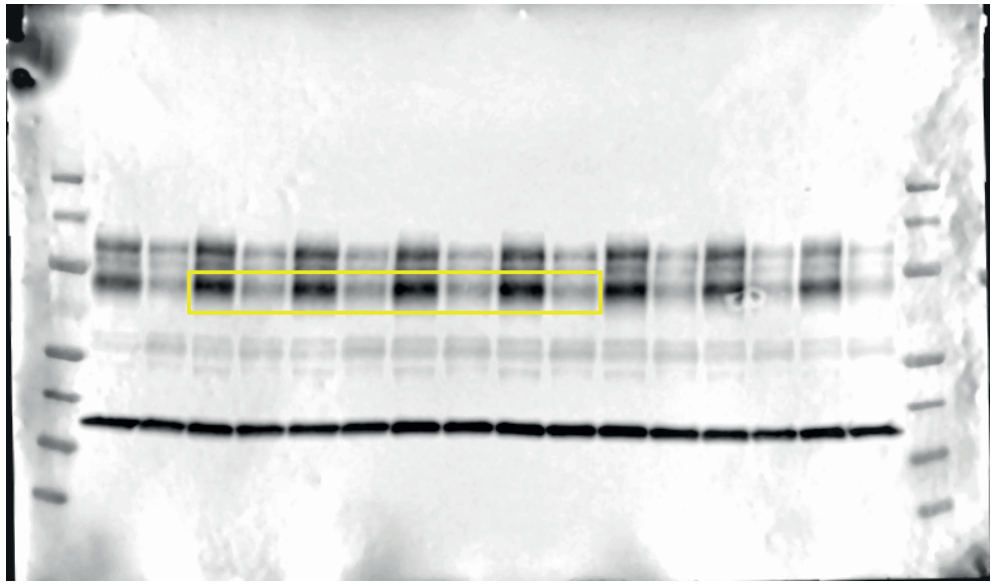

Composite_Green_Kv1.2

Raw images of western blots in Figure 3

Whole brain

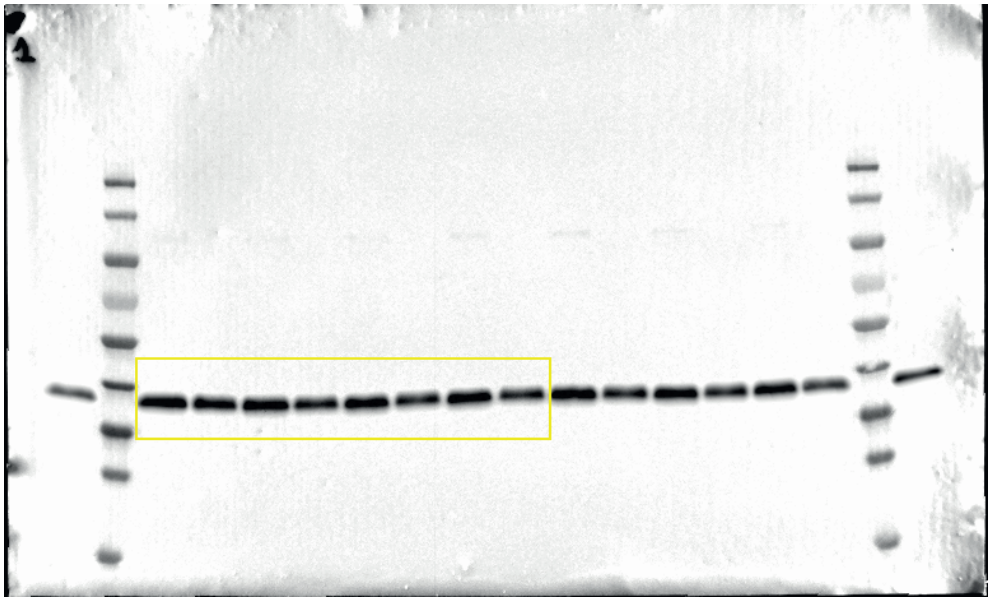

Composite_red_GAPDH

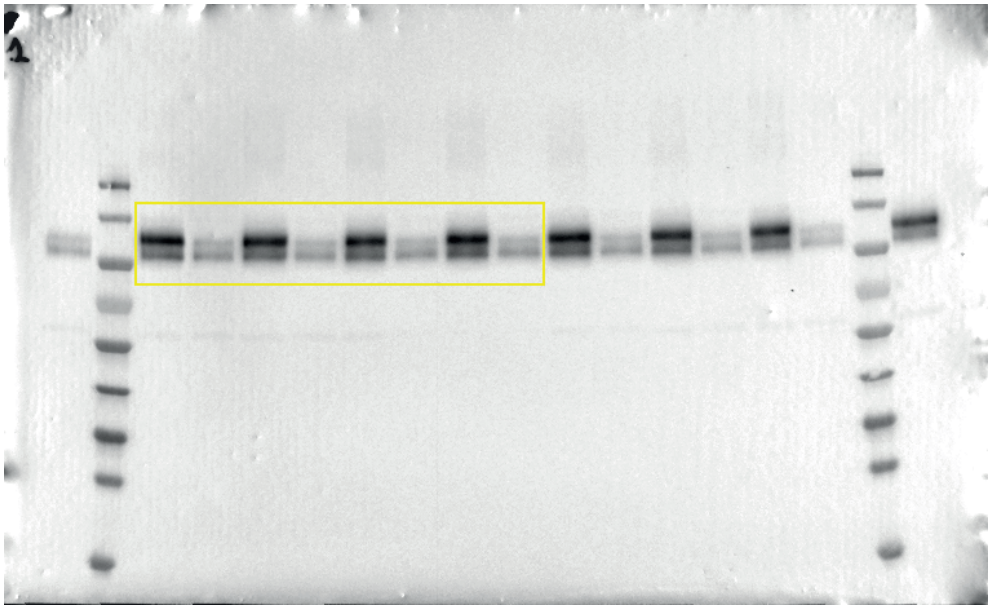

Composite_green_PSD93

Hippocampus

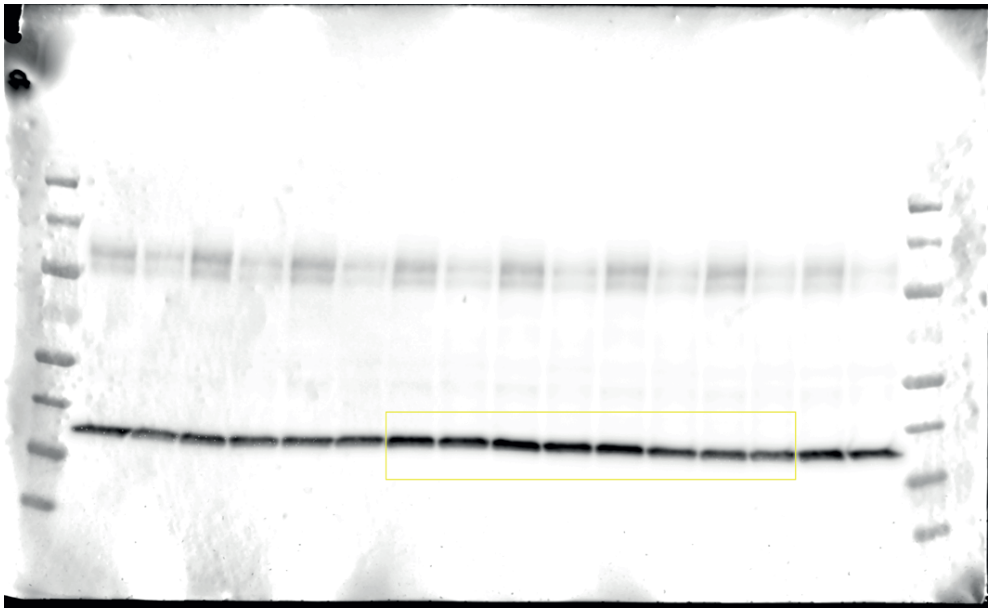

Composite_red_GAPDH

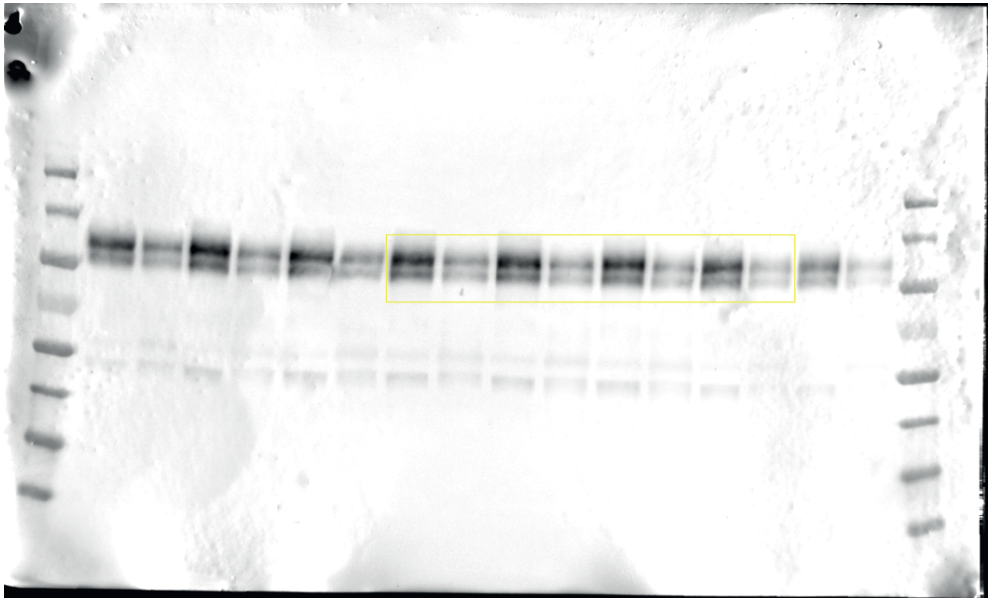

Composite_green_PSD93

Raw images of western blots in Figure 4

Whole brain

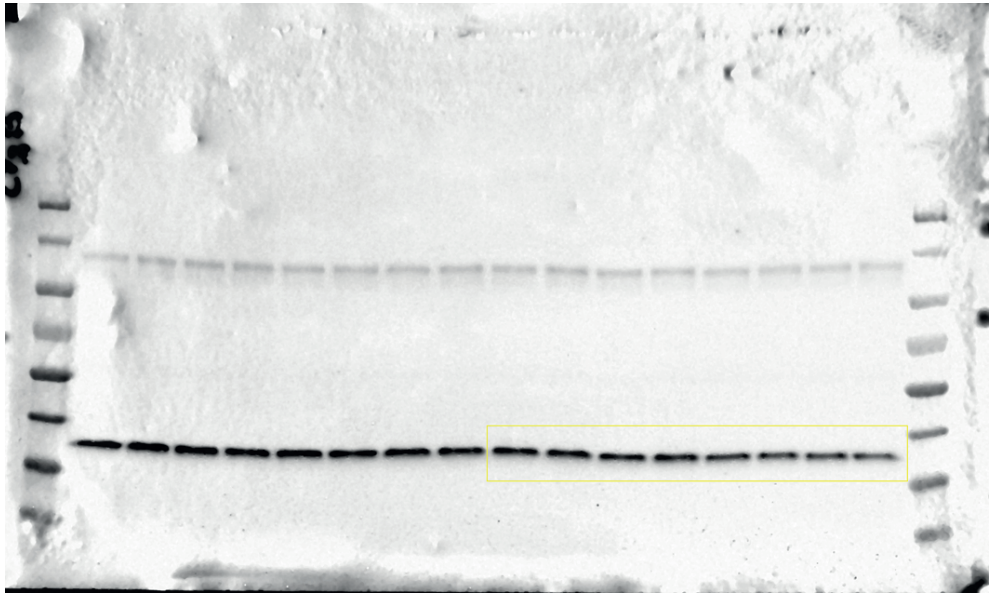

Composite_red_GAPDH

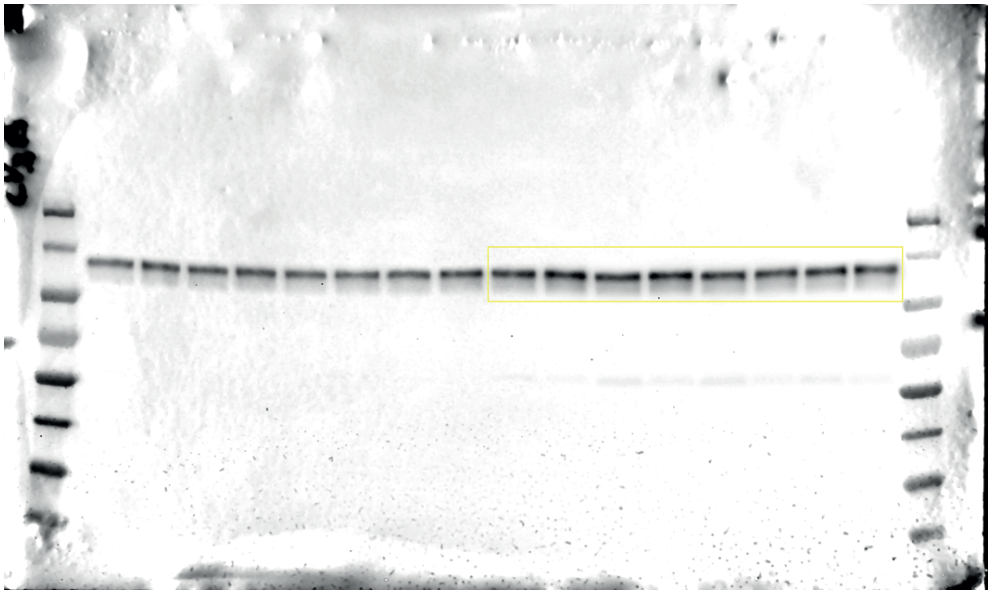

Composite_green_Kv2.1

Hippocampus

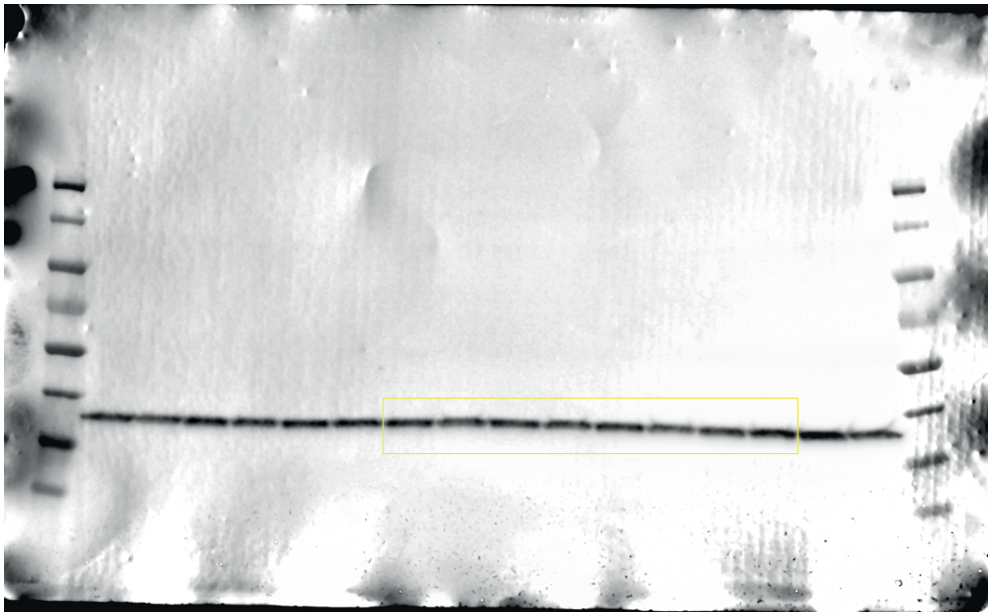

Composite_red_GAPDH

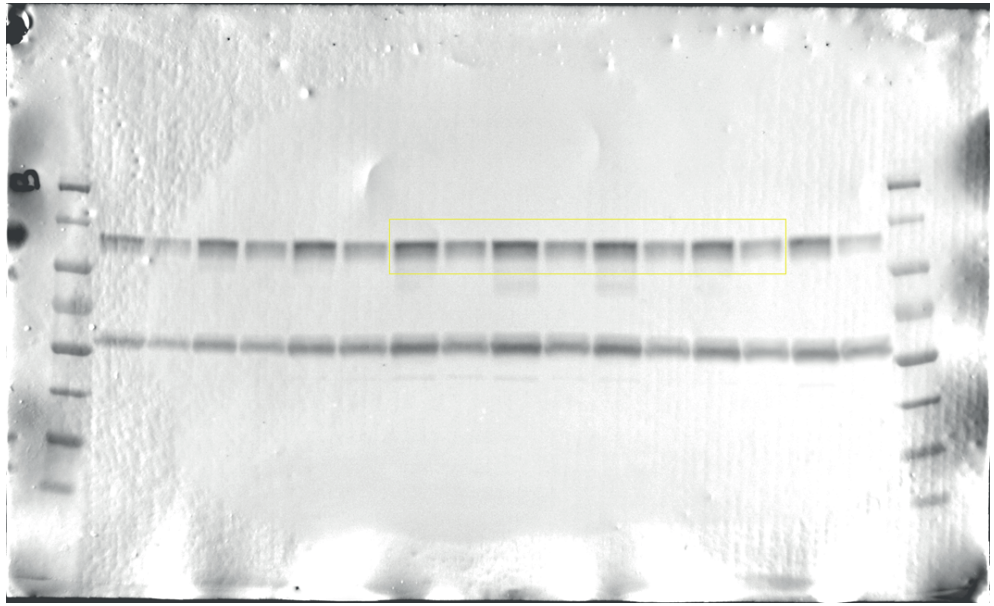

Composite_green_Kv2.1

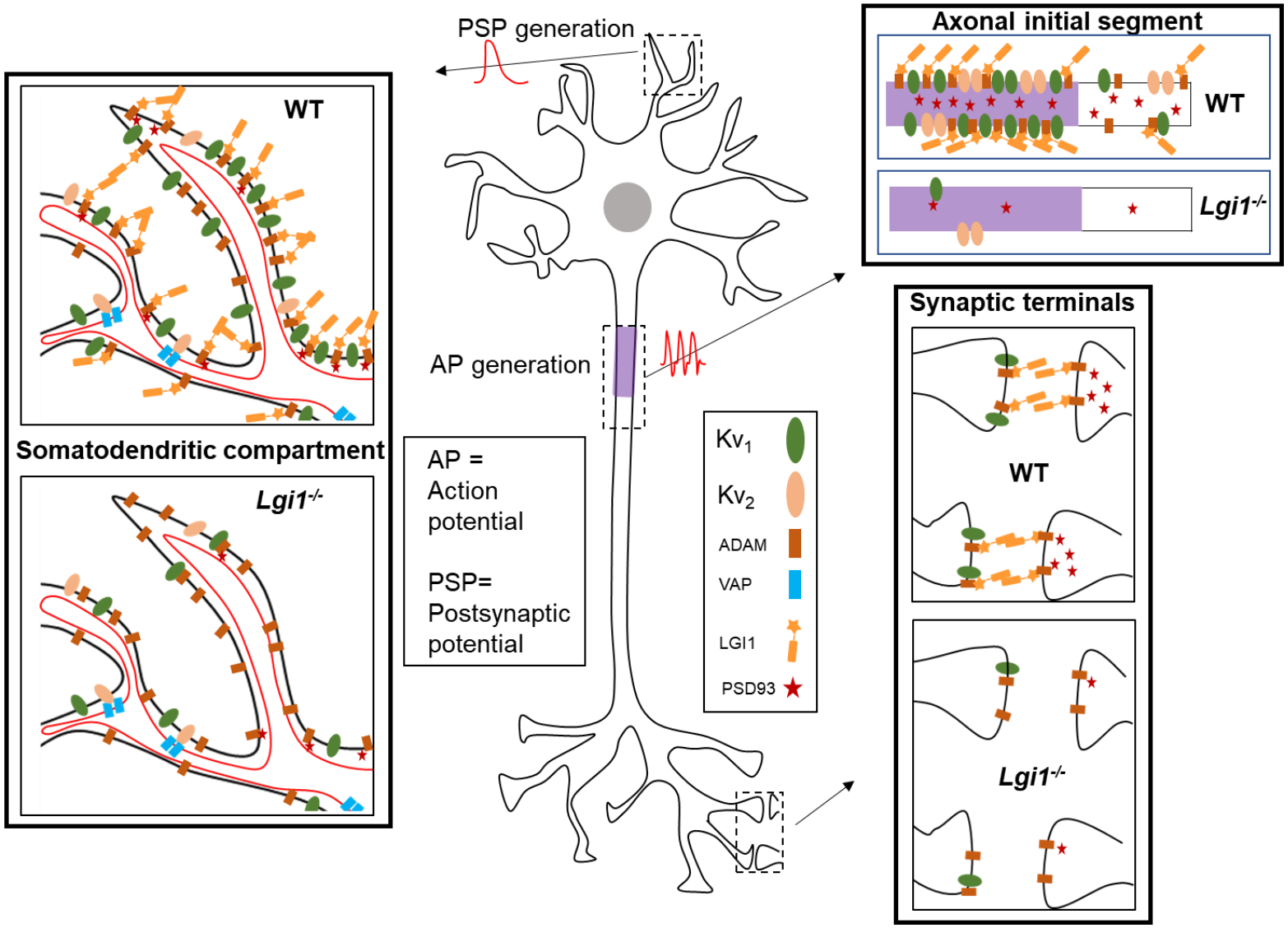
WT
Somatodendritic compartment
Lgi1-/-
PSP generation
AP generation
AP = Action potential
PSP= Postsynaptic potential
Kv1
Kv2
ADAM
VAP
LGI1
PSD93
Axonal initial segment
WT
Lgi1-/-
Synaptic terminals
WT
Lgi1-/-